



**US Army Corps
of Engineers®**
Engineer Research and
Development Center



Assessment of LiDAR- and Photogrammetry- based Airfield Roughness Profiling Techniques

Andrew B. Ward, J. Kent Newman, and G. Bryan Herring IV

June 2019



The U.S. Army Engineer Research and Development Center (ERDC) solves the nation's toughest engineering and environmental challenges. ERDC develops innovative solutions in civil and military engineering, geospatial sciences, water resources, and environmental sciences for the Army, the Department of Defense, civilian agencies, and our nation's public good. Find out more at www.erdcl.usace.army.mil.

To search for other technical reports published by ERDC, visit the ERDC online library at <http://acwc.sdp.sirsi.net/client/default>.

Assessment of LiDAR- and Photogrammetry-based Airfield Roughness Profiling Techniques

Andrew B. Ward and J. Kent Newman

*Geotechnical and Structures Laboratory
U.S. Army Engineer Research and Development Center
3909 Halls Ferry Road
Vicksburg, MS 39180-6199*

G. Bryan Herring IV

*Coastal and Hydraulics Laboratory
U.S. Army Engineer Research and Development Center
3909 Halls Ferry Road
Vicksburg, MS 39180-6199*

Final report

Approved for public release; distribution is unlimited.

Prepared for U.S. Army Engineer Research and Development Center
Vicksburg, MS 39180-6199

Under Project Number 465397

Abstract

The measurement of surface roughness is one of the factors necessary for determining stable landing and take-off conditions on airfields. The U.S. Army identified a need for rapid and precise assessment of airfield surface roughness without grossly inhibiting aircraft traffic. The present standard of roughness measurement includes the use of cumbersome ground vehicle-based inertial profilers or slow-speed profilographs. The use of Unmanned Aerial System (UAS) based photogrammetry for remote assessment has been highly successful and the data products derived from these systems are useful to surface roughness measurements. Roughness parameters like the Boeing Bump Index and International Roughness Index can be calculated using 3-D reconstructed surface data derived from photogrammetric techniques. Roughness parameters can also be calculated using the surface obtained by Light Detection and Ranging (LiDAR) systems. While LiDAR techniques are highly accurate and robust, they are often cost-prohibitive. The assessment of photogrammetry-based alternatives to LiDAR systems is required to satisfy airfield roughness measurement needs. Findings herein show that photogrammetric techniques can provide sufficient surface profiles for use in roughness measurement. This report compares multiple photogrammetric software packages for best correlation to actual surface profiles and concludes with a preferred method of surface roughness measurement using UAS-based photogrammetry.

DISCLAIMER: The contents of this report are not to be used for advertising, publication, or promotional purposes. Citation of trade names does not constitute an official endorsement or approval of the use of such commercial products. All product names and trademarks cited are the property of their respective owners. The findings of this report are not to be construed as an official Department of the Army position unless so designated by other authorized documents.

DESTROY THIS REPORT WHEN NO LONGER NEEDED. DO NOT RETURN IT TO THE ORIGINATOR.

Contents

| | |
|--|-----------|
| Abstract | ii |
| Figures and Tables | v |
| Preface | vi |
| 1 Introduction | 1 |
| 1.1 Problem | 1 |
| 1.2 Objective and scope | 1 |
| 2 Literature Review | 2 |
| 2.1 Photogrammetry | 2 |
| 2.1.1 Alignment | 2 |
| 2.1.2 Georectification | 4 |
| 2.1.3 Dense reconstruction | 4 |
| 2.1.4 Product generation | 5 |
| 2.2 LiDAR | 7 |
| 2.3 Roughness measurement..... | 8 |
| 2.3.1 Boeing Bump Index..... | 8 |
| 2.3.2 International Roughness Index | 9 |
| 3 Equipment Overview | 12 |
| 3.1 UAS-based equipment..... | 12 |
| 3.2 Mobile LiDAR equipment..... | 14 |
| 4 Field Test Methods | 18 |
| 4.1 UAS EO data collection | 19 |
| 4.2 Simulated UAS LiDAR data collection..... | 21 |
| 5 Data Analysis | 24 |
| 5.1 3D reconstruction..... | 24 |
| 5.1.1 Agisoft Photoscan workflow..... | 24 |
| 5.1.2 Pix4D Mapper workflow..... | 25 |
| 5.2 LiDAR post-processing..... | 27 |
| 6 Results | 28 |
| 6.1 LiDAR analysis | 29 |
| 6.2 Photogrammetry analysis..... | 32 |
| 6.2.1 Photoscan reconstruction | 32 |
| 6.2.2 Pix4D reconstruction | 42 |
| 7 Conclusions and Recommendations | 47 |
| 7.1 Conclusions..... | 47 |
| 7.2 Recommendations | 48 |

References.....49

Report Documentation Page

Figures and Tables

Figures

| | |
|--|----|
| Figure 1. Pixel-level dense reconstruction. | 5 |
| Figure 2. Product generation screenshots..... | 5 |
| Figure 3. Boeing roughness criteria from 1995 to present..... | 9 |
| Figure 4. IRI quarter-car model. | 10 |
| Figure 5. TurboAce Matrix-E quadcopter UAS. | 12 |
| Figure 6. UAS radio equipment. | 13 |
| Figure 7. Matrix T-motor brushless motor..... | 14 |
| Figure 8. Riegl VMZ 2000 LiDAR System..... | 15 |
| Figure 9. Laser system mounted to extended telehandler..... | 16 |
| Figure 10. Close up of laser system mounted to aluminum frame..... | 17 |
| Figure 11. Google Earth image of the Camp Rudder area..... | 18 |
| Figure 12. Survey mission planning screenshot. | 19 |
| Figure 13. GCP spacing on sand-asphalt surface..... | 20 |
| Figure 14. Telehandler pallet fork and ratchet-strap mounting system..... | 21 |
| Figure 15. LiDAR survey path on sand-asphalt surface. | 23 |
| Figure 16. Cross-section spacing on sample surface..... | 28 |
| Figure 17. LiDAR data with intensity colorization..... | 29 |
| Figure 18. Photoscan data with EO colorization..... | 33 |
| Figure 19. Photoscan vs. LiDAR data using BBI and IRI on sand-asphalt. | 37 |
| Figure 20. Photogrammetry vs. LiDAR using BBI and IRI on dirt. | 38 |
| Figure 21. Photogrammetry vs. LiDAR using BBI and IRI on main runway asphalt. | 40 |
| Figure 22. Photogrammetry vs. LiDAR using BBI and IRI on concrete..... | 41 |
| Figure 23. Pix4D data with EO colorization..... | 42 |
| Figure 24. Pix4D vs. LiDAR data using BBI and IRI on sand-asphalt..... | 45 |

Tables

| | |
|--|----|
| Table 1. Average BBI and IRI data for Camp Rudder surfaces. | 31 |
| Table 2. Photogrammetry analysis COD and rRMSE values. | 35 |

Preface

The work was performed by the Airfields and Pavements Branch (GMA) of the Engineering Systems and Materials Division (GM), U.S. Army Engineer Research and Development Center, Geotechnical and Structures Laboratory (ERDC-GSL). At the time of publication, Dr. Timothy W. Rushing was Chief, CEERD-GMA; Mr. Justin Strickler was Acting Chief, CEERD-GM; and Mr. R. Nicholas Boone, CEERD-GZT, was the Technical Director for Force Projection and Maneuver Support. The Deputy Director of ERDC-GSL was Mr. Charles W. Ertle II, and the Director was Mr. Bartley P. Durst.

COL Ivan P. Beckman was the Commander of ERDC, and Dr. David W. Pittman was the Director.

1 Introduction

1.1 Problem

Airfield pavement surface irregularities can cause unsafe operations for aircraft. A precise measurement of pavement roughness is necessary to quantify the impact of pavement roughness on aircraft operations. Current standard procedures consist of using ground vehicle-based inertial profilers and slow-speed push-behind profilographs. The operation of these devices is tedious and time consuming. An accurate, timely, and cost-effective alternative to pavement profilographs and inertial profilers is desired to insure safe aircraft operations without grossly inhibiting aircraft traffic. Photogrammetry and Light Detection and Ranging (LiDAR) platforms may prove to be sufficient for pavement surface measurement.

1.2 Objective and scope

The primary objective of this research was to develop remote pavement assessment techniques in a permissive environment over a range of pavement qualities. The following three objectives were identified as necessary to develop such techniques:

1. Evaluate the use of unmanned aerial system (UAS) based photogrammetry techniques in surface reconstruction.
2. Compare photogrammetry findings to existing LiDAR techniques for accuracy and correlation on at least four unique surfaces.
3. Directly compare two photogrammetric reconstruction techniques; namely, Agisoft Photoscan and Pix4D Mapper.

To accomplish these objectives, the roughness characteristics of various pavement surfaces were analyzed in the Camp Rudder area at Eglin Air Force Base.

2 Literature Review

Surface roughness can be quantified in many ways, from straightedge-based methods to photogrammetry and LiDAR-based methods. Modern photogrammetric techniques are cost-effective and highly adaptable. LiDAR techniques are much more precise and much less cost-effective. The following sections review these various techniques.

2.1 Photogrammetry

Photogrammetry is the science of calculating the distance between points on a three-dimensional (3-D) surface from measurements made on two-dimensional (2-D) photographs. This act allows for the reconstruction of a 3-D scene using only 2-D imagery. The problem of 3-D reconstruction is difficult and long studied. To perform a pixel-level reconstruction of a 3-D scene requires either ample time or immense computational resources. Three-dimensional reconstruction is made even more difficult by the diverse makeup of the computational requirements of the various steps of the 3-D reconstruction process. For example, mesh generation has strict memory and CPU requirements, where pixel-level dense reconstruction algorithms, like multi-view stereo, have heavy graphics processing unit (GPU) requirements. Recent advances in the parallel processing of 2-D imagery for the purpose of 3-D reconstruction allows for the timely reconstruction of a 3-D scene.

The algorithms supporting the process of 3-D reconstruction are complex and time consuming; such that, the use of commercial-off-the-shelf (COTS) photogrammetry software is often preferred to developing in-house solutions. Examples of popular COTS 3-D reconstruction software are Agisoft Photoscan, Pix4D Mapper, and Bentley ContextCapture. Steps necessary to complete the 3-D reconstruction process as they relate to the present work are detailed below. The process can be separated into five categories: data collection, Structure from Motion (SfM), georectification with ground control, dense reconstruction, and product generation (Verhoeven et al. 2013).

2.1.1 Alignment

In the alignment, or Structure from Motion (SfM), step, 2-D photos are aligned with each other based on detected unique features present in

multiple photos. The principal steps in the alignment phase have been discussed in various works (Ullman 1979, Westoby et al. 2012, Verhoeven et al. 2013) even dating as far back as the 1950s where the process was known as the “kinetic depth effect” (Wallach and O’Connell 1953).

2.1.1.1 Feature detection

The first part of alignment is feature detection. In this step, interest points (IPs) are detected that are highly repeatable, i.e., invariant, in the 2-D photos, to rotation and distortion. An IP is a point in the image that is distinct and also has a distinct neighborhood of points. Multiple IPs are needed in each 2-D image for sufficient alignment.

2.1.1.2 Feature description

The next step comprises the computation of feature descriptors, describing the IPs and their local area. Descriptor information typically relies on the intensity profile of the local area. Popular feature detection techniques include descriptor matching. Many time-optimized feature detection/description techniques are available:

- Speeded Up Robust Features (SURF) (Bay et al. 2008)
- Scale-invariant Feature Transform (SIFT) (Lowe 1999)
- Binary Robust Invariant Scalable Keypoints (BRISK) (Leutenegger et al. 2011)
- Features from Accelerated Segment Test (FAST) (Rosten and Drummond 2005)

2.1.1.3 Descriptor matching

Following the detection and description of unique IPs, individual IP descriptors are matched in multiple images. This is performed by first defining the Euclidean distance between descriptors in a pair of images. Shorter Euclidean distance between two considered descriptors indicates likely matching. Robust outlier analysis is then performed to cull false positives. The most popular such outlier removal approach is Random Sampling Consensus (RANSAC) (Fischler and Bolles 1980). In this approach, a least-squares straight line is fit to a randomly sampled set of matched IPs until a pre-determined goodness-of-fit threshold is met.

2.1.1.4 Triangulation

Once inlier IPs are selected, their positions are determined through observations of the individual IPs in two or more images. This procedure allows for the creation of a local coordinate system scaled in metric or imperial units.

2.1.1.5 Bundle adjustment

The minimization of calculated re-projection errors with respect to intrinsic and extrinsic camera parameters is performed here (Triggs et al. 1999). This step minimizes actual error in the 3-D scene reconstruction in all images simultaneously, as opposed to the pair-wise matching performed in previous steps.

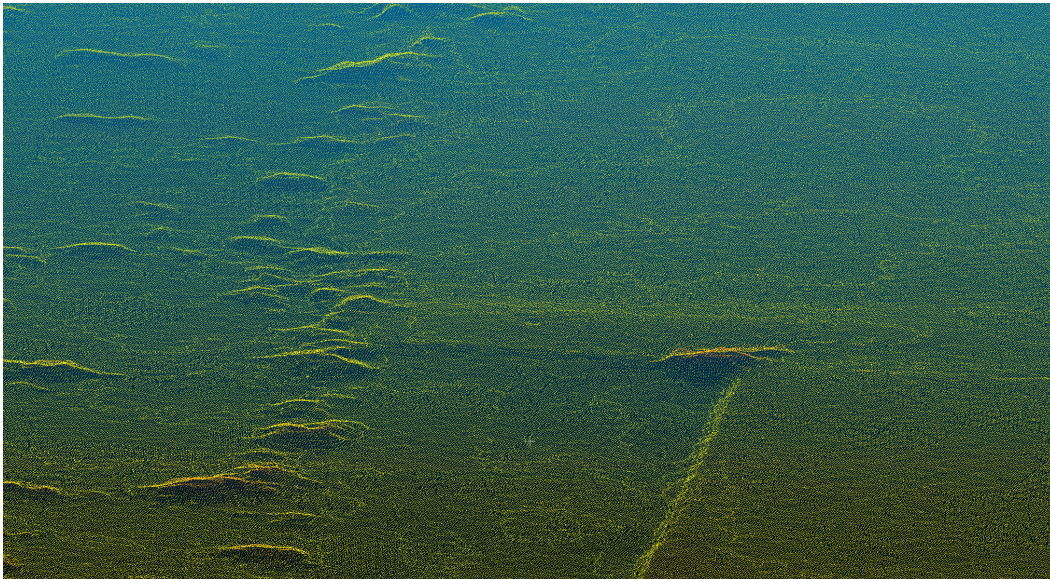
2.1.2 Georectification

Ground control points (GCPs) are used to translate the local SfM coordinate system into a global coordinate system like World Geodetic System 1984 (WGS84), Universal Transverse Mercator (UTM), etc. Furthermore, scaling and geolocation accuracy will depend heavily on ground control accuracy and placement. Pattern recognition features are available in popular 3-D reconstruction software (Pix4D and Photoscan) to use automatically detectable GCPs in scene reconstruction.

2.1.3 Dense reconstruction

A 3-D scene is reconstructed at the pixel-level (Figure 1), as opposed to the feature level in the previous steps. Typical pixel-level dense reconstruction is performed using a dense multi-view stereo (MVS) approach. In general the MVS approach consists of generating candidate pixel pairs from multiple images and determining the probability of matching them using photo-consistency measures. Variability within COTS software in the 3-D reconstruction process is likely due to proprietary implementations of this step. Most photogrammetric software will use a type of MVS for pixel-level dense reconstruction. The MVS algorithm is usually complemented by a camera projection model like the pinhole camera model. The pinhole camera model incorporates the extrinsic and intrinsic camera properties into a projection matrix. The projection matrix includes properties like focal length, principal point, and skew (Furukawa and Hernandez 2015).

Figure 1. Pixel-level dense reconstruction.



2.1.4 Product generation

Once pixel-level 3-D reconstruction is accomplished, data products like textured meshes (Figure 2a), orthomosaics (Figure 2b), and digital elevation models (DEMs, Figure 2c) can be generated.

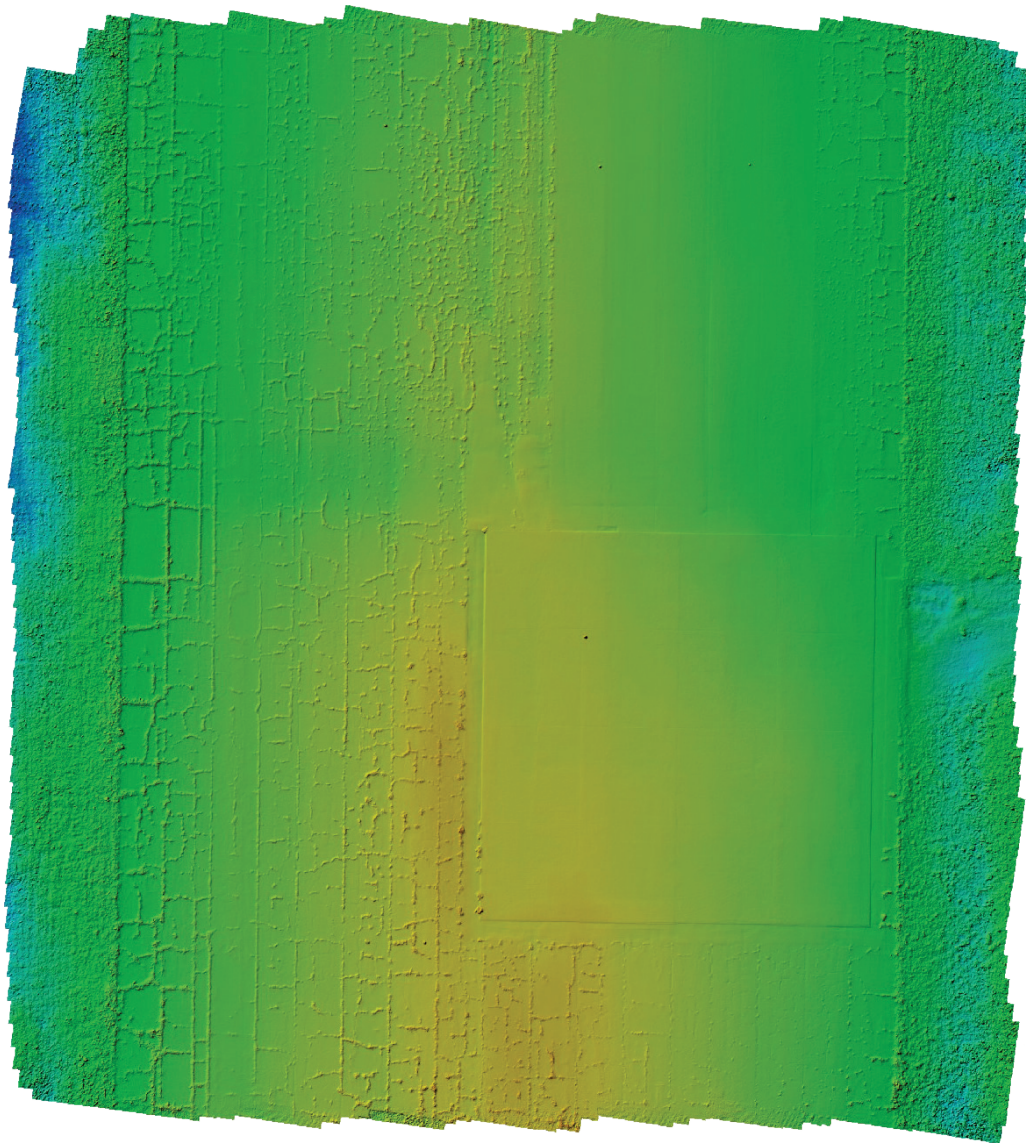
Figure 2. Product generation screenshots.



a) Textured mesh



b) Georeferenced orthomosaic



c) Georeferenced DEM

2.2 LiDAR

Light Detection and Ranging, or LiDAR, is a laser-based return time survey technique. One of the first uses of laser-based technology as a survey technique was performed in the field of meteorology by Goyer and Watson (1963) just three years after the invention of the laser by T. H. Maiman (1960).

In modern high-resolution LiDAR systems, a laser source produces a beam of light that illuminates the surface in a small area, and reflected light is detected by an onboard photodetector. Based on data collected by the photodetector, measurements like return time and light intensity are made

and used to map, or range, the surface. Among modern LiDAR systems are two general categories: topographic and bathymetric. Topographic LiDAR is used to quantify the topology of land surfaces and typically uses a laser source from the near-infrared portion of the electromagnetic (EM) spectrum. By contrast, bathymetric LiDAR is used to measure the bathymetry of seafloors and riverbeds and typically uses a laser source from the green portion of the EM spectrum in order to penetrate the water's surface.

2.3 Roughness measurement

Pavement roughness is quantified as the change in pavement surface from a theoretically uniform plane. Deviations in airfield pavement surface roughness can negatively affect the ride quality of aircraft during landing and takeoff operations. Even small variations in pavement roughness can lead to aircraft failure on the lead up to arrester systems where aircraft hooks require very uniform and smooth pavements.

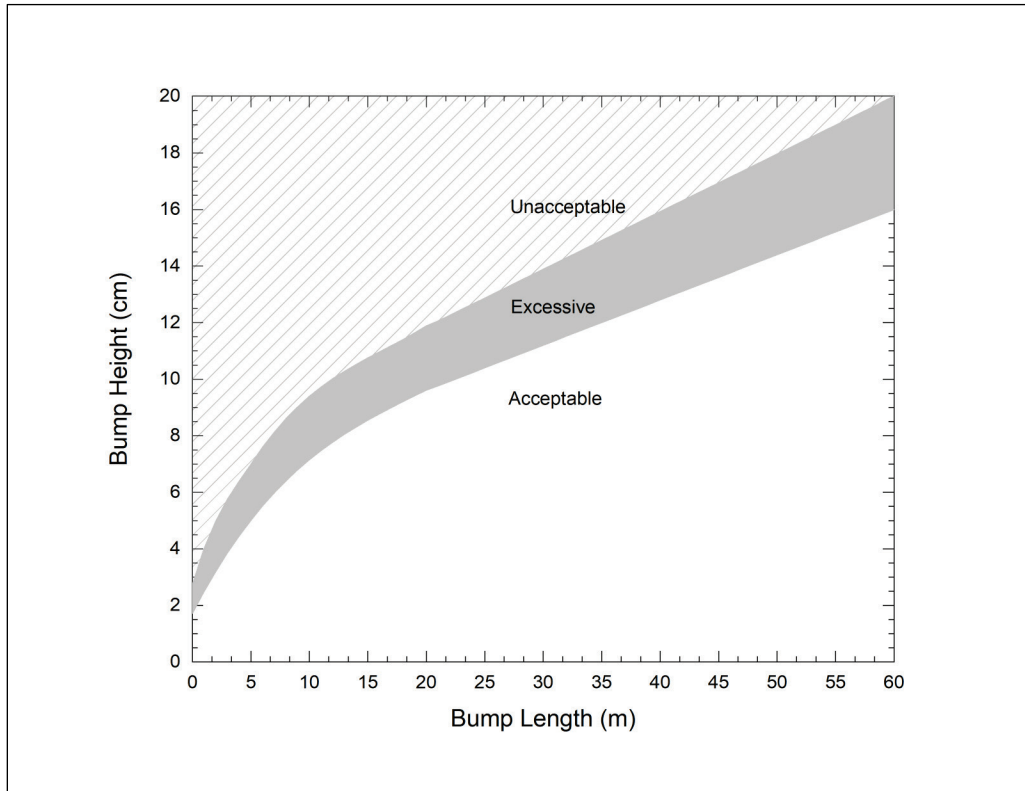
For aircraft, the standard for pavement roughness measurement is the Boeing Bump Index (BBI). For highways, roughness is typically determined by use of the International Roughness Index (IRI). The IRI parameter is also used in airfield roughness measurements.

2.3.1 Boeing Bump Index

The original Boeing Bump criteria was developed by Boeing in an effort to better quantify runway surface roughness standards (DeBord 1995). This criteria was further developed by the FAA into the BBI (FAA 2009). The BBI is not a measure of roughness wavelength, but rather a measure of single-event bumps.

The original Boeing criteria, from 1975-1994, were developed from a combination of instrumented Boeing 737 operations and numerical models of Boeing 737 aircraft operating on a testbed (DeBord 1995). Operational data collected further refined the Boeing criteria in 1995 to only three categories: acceptable, excessive, and unacceptable (Figure 3).

Figure 3. Boeing roughness criteria from 1995 to present.

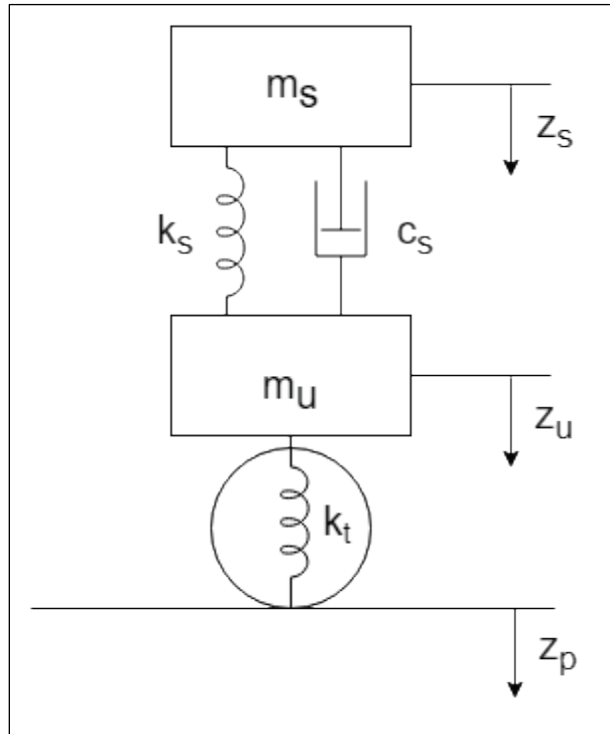


The FAA's development of the BBI was in an effort to simplify the Boeing Bump criteria's use. Following FAA AC 150/5380-9, the BBI is determined by computing the ratio of measured bump height and the limit of acceptable bump height from Figure 3 for all sample points in the surface profile. The largest value for each sample point in the profile is the BBI for that point. A BBI of one or less falls into the acceptable area and a BBI greater than one is either in the excessive or unacceptable zone.

2.3.2 International Roughness Index

The IRI is an index describing the roughness of a single wheel-track surface using a quarter-car model. The quarter-car model consists of a system of springs and masses approximating a single tire rolling across a surface (Figure 4).

Figure 4. IRI quarter-car model.



From Figure 4, where m_s is the sprung mass (vehicle mass supported by a single tire), m_u is the un-sprung mass (mass of wheel and axel assembly supporting a single tire); k_s is the spring constant controlling the springing action of the vehicle suspension; c_s is the damping constant controlling the dampening action of the vehicle suspension; k_t is the spring constant controlling the springing action of the vehicle's single tire; z_s is the displacement of the sprung mass; z_u is the displacement of the un-sprung mass; and z_p is the displacement of the tire from the surface profile.

Given the simplified model in Figure 4, the equations of motion for such a system can be easily determined by Newtonian (Sayers 1988), Lagrangian, or Hamiltonian means and follow in Equations 1 and 2 below.

$$m_s \ddot{z}_s + k_s(z_s - z_u) + c_s(\dot{z}_s - \dot{z}_u) = 0 \quad (1)$$

$$m_u \ddot{z}_u - k_s(z_s - z_u) - c_s(\dot{z}_s - \dot{z}_u) = k_t(z_p - z_u) \quad (2)$$

The two second-order ordinary differential equations (ODEs) above, when decomposed into four first-order ODEs, can be time-integrated numerically to yield the motion of the suspension over the entire profile.

The accumulated suspension motion, $\sum|z_s - z_u|$, is divided by the total length of the profile and reported as the IRI (Sayers 1995). The IRI is reported in either metric units of meters per kilometer (*m/km*) or imperial units of inches per mile (*in./mile*).

The next chapter explores the equipment and technologies employed to quantify surface roughness in such a way as to support the input data requirements of the BBI and IRI.

3 Equipment Overview

Photogrammetric analysis can be performed with numerous types of optical sensors: electro-optical (EO), multi-spectral, hyper-spectral, longwave infrared, etc. This study uses EO sensors to return red-green-blue (RGB) data for a given test surface. LiDAR data, on the other hand, requires the use of a laser transmission and return receiver setup. The LiDAR sensor does not return EO data like a normal camera, but does provide the light intensity of the laser returns. The equipment used to test these various methods are detailed below.

3.1 UAS-based equipment

Aerial data were collected using the TurboAce Matrix-E quadcopter UAS (Figure 5). The Matrix was equipped with a 2-axis AllSteady gimbal at the front that carries the payload; in this case, an EO sensor. The 2-axis gimbal allowed for the payload to be in a rolling and tilting action, but not in a panning action. The Matrix itself had to provide the panning action, if necessary. The AllSteady 2-axis gimbal, even with this limitation, was sufficient to provide consistent survey imagery while the payload was pointed nadir (directly below the UAS).

Figure 5. TurboAce Matrix-E quadcopter UAS.



The EO sensor used during this work was the Sony A6000 featuring a 24.3 megapixel (MP) CMOS image sensor with a full image resolution of 6000×4000 pixels. The A6000 was also equipped with Sony's e-mount lens system, allowing for a wide range of lenses to be used with the sensor at varying focal lengths. A Sony SELP1650 16-50 mm Power Zoom lens was used during this research. The SELP1650 allows for a wide range of focal lengths to be tested; however, the SELP1650 required manual focusing before flight. Typically a target was placed at the desired distance and focused on the ground before being attached to the Matrix.

The Sony A6000 among other components was connected to the drone's Pixhawk 1 flight controller. The Pixhawk sent vital telemetry data to the ground station to allow for accurate survey routing. GPS data were fed into the Pixhawk's telemetry system using a 3DR Neo 7 GPS module.

A Futaba T14SG radio controller (Figure 6a) provided control over the drone to a ground-based pilot. The T14SG acted as a transmission source, and the drone was equipped with Futaba R7008SB to act as a radio receiver. The safe transmission range of this setup was approximately 3,000 ft.

Figure 6. UAS radio equipment.



a) Futaba radio controller, b) Connex transmitter, c) Connex receiver.

Precise control over the Matrix was aided by a first-person view (FPV) receiver and transmitter system in the form of the Amimon Connex HD video downlink (Figure 6b and 6c). The Connex system provided the ground station with whatever was being captured by the A6000, including image stills of 1080p 60 frames per second (fps) video. The Matrix was equipped with a transmitter that took input from the A6000's HDMI port.

Flight was facilitated by four Tiger Motor U5 400kv brushless motors (Figure 7), each equipped with a Tiger 15x5 carbon fiber prop. The four motors were each controlled by a 40-amp SimonK electronic speed controllers (ESCs). Power on board the Matrix was provided by a single Tattu LiPo 6s 16,000 mAh battery. Flight time with the A6000 payload was approximately 18 min.

Figure 7. Matrix T-motor brushless motor.



3.2 Mobile LiDAR equipment

LiDAR data were collected using the Riegl VMZ 2000 Hybrid Mobile Lidar System (Figure 8). This system is a hybrid mobile laser mapping system for three-dimensional static and kinematic data acquisition. The Riegl VMZ 2000 couples a Riegl Z-line laser scanner (VZ 2000) with a POSLV GPS/IMU (inertial measurement unit) system for precise post-processed position data along with heave, pitch, and roll information. A Nikon D800 DSLR EO camera is mounted to the laser for image data acquisition that can be used to colorize the laser-based point cloud with RGB data. For calibration, the camera was GPS synchronized with the POSLV system.

Figure 8. Riegl VMZ 2000 LiDAR System.



The laser system was mounted atop a custom fabricated 14-ft-tall aluminum tower that was then fitted to a telehandler to allow for data collection at simulated UAS altitudes (Figure 9). The aluminum frame tower had a flat top made of an aluminum grate. A rectangular body made of 80-20 aluminum framing was mounted to the aluminum grate at the top of the tower and two 80-20 frame arms were mounted at 180 deg apart on the long axis of the larger frame (Figure 10). Two Trimble antennas interfacing with the POSLV GPS system were mounted at the frame arms. The laser system was fitted into a shock absorbent horizontal mount that was then bolted into a machined aluminum plate fixed to the front face of the tower frame. The laser system is powered by a 2,000-W gas-powered generator mounted at the base of the tower.

Figure 9. Laser system mounted to extended telehandler.



Figure 10. Close up of laser system mounted to aluminum frame.



A single 100-ft-long Ethernet cable was connected between the laser system and a Windows-based laptop computer in order to facilitate data acquisition and storage during collection.

A Trimble R8 GNSS-3 GPS tripod system was placed on a temporary benchmark point of known position. The benchmark point was chosen to be as close to the testing area as possible. The Trimble R8 system collected 1-Hz GPS data throughout the data collect for use in post-processing of trajectory data. The Trimble base station was set up at least an hour prior to data collection.

4 Field Test Methods

Data collection efforts at Camp Rudder, Eglin AFB (Figure 11), took place during two events. The first, a UAS EO data collection, took place 24-25 January 2018. The second, a simulated UAS LiDAR data collection, took place on 13 February 2018. Weather conditions were approximately the same for both data collection events. Some difference was noted in the rutting on the dirt surface but was not found to be sufficient to preclude the dirt surface from full analysis.

Figure 11. Google Earth image of the Camp Rudder area.

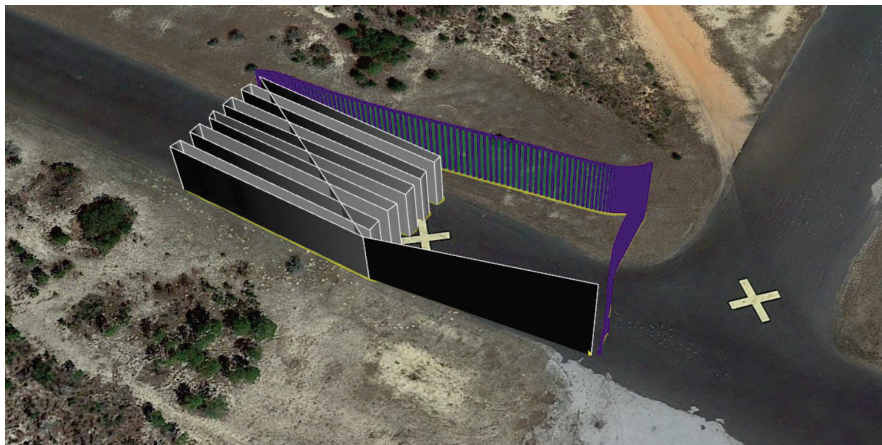


Four pavement surface types were tested at the Camp Rudder airfield: sand-asphalt, dirt, main runway asphalt, and concrete pad. These surfaces provide a varying roughness profile in order to test the EO and LiDAR-based measurement techniques.

4.1 UAS EO data collection

Two-dimensional photo data is collected by two UAS operators. One operator runs a base station that controls GPS waypoint targets for the UAS. The second operator handles UAS flight using a radio controller. The TurboAce Matrix-E quadcopter (Figure 5) is used to carry an optical sensor at altitude for the survey. Waypoint missions are configured before a survey by the base station operator (Figure 12) and manual takeoff and landings are handled by the UAS flight operator.

Figure 12. Survey mission planning screenshot.



Two-dimensional EO data were collected by a Sony A6000 camera using a variable zoom lens set to 35mm. The A6000 collected EO data at a resolution of approximately 24 megapixels for an image resolution of 6000×4000 pixels. Photos were taken in such a way as to allow for the overlap of images in the direction of travel (front-lap) and in the direction transverse to travel (side-lap). Image overlap, ω , is a function of image capture displacement, d , flight altitude, h , and field of view (FOV), α (Equation 3).

$$\omega = 1 - \frac{d}{2h} \cot\left(\frac{\alpha}{2}\right) \quad (3)$$

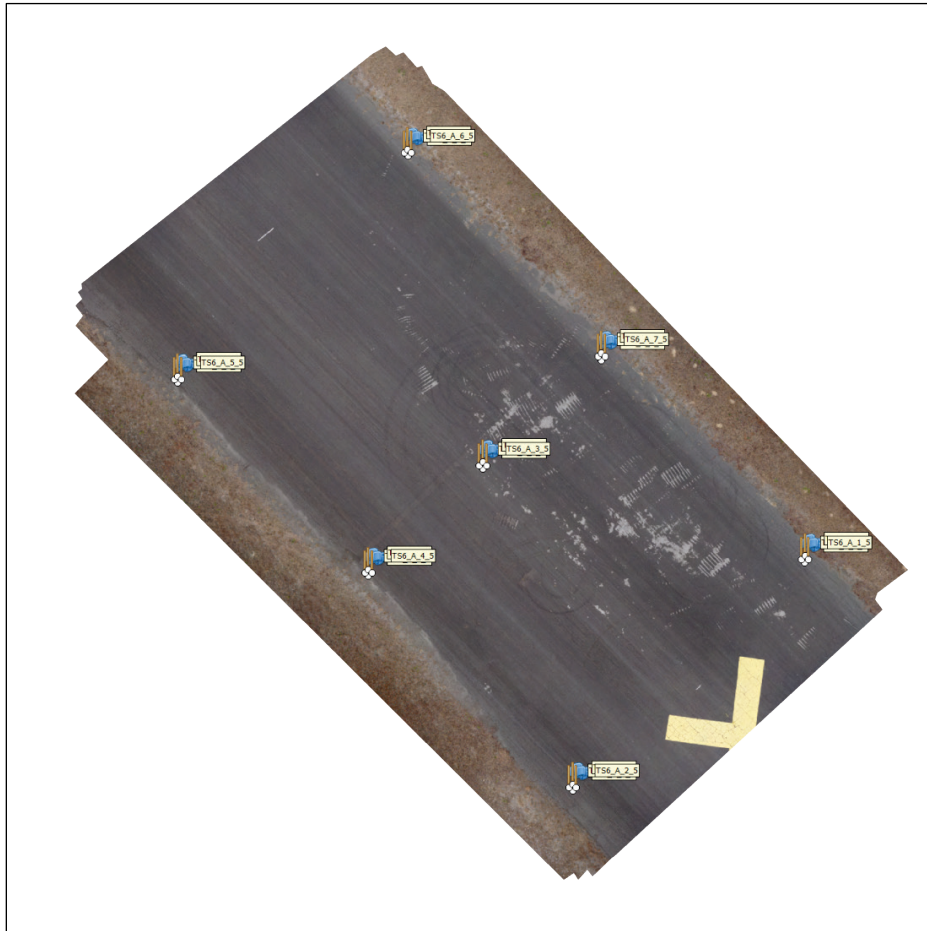
Side-lap is calculated by using the horizontal FOV, and front-lap is calculated using the vertical FOV. Using the Sony A6000 equipped with a 35-mm lens, the horizontal FOV is 54.4° , and the vertical FOV is 37.8° . Typically, the overlap equation is solved for the image capture displacement and used to determine an intervalometer time; such that, if

the speed of the UAS, v , is known and the distance is calculated using Equation 3, then the time between image captures, t , is calculable (Equation 4).

$$t = \frac{2h}{v} (1 - \omega) \tan\left(\frac{\alpha}{2}\right) \quad (4)$$

GCP locations were collected in the field by a trained Trimble operator and saved in the UTM coordinate system (Northing, Easting, and Elevation). GCPs were spaced such that they covered the entire survey area uniformly (Figure 13).

Figure 13. GCP spacing on sand-asphalt surface.



Large GCP targets were used so that they were visible in both low (50 ft) and high (>200 ft) altitude flights. The GCP targets used were each 2 ft x 2 ft and made from 14-gauge steel. The targets were painted in a checkboard pattern so that the center was visible even through image blurriness or distortion.

4.2 Simulated UAS LiDAR data collection

The VMZ 2000 laser system, while typically operated off the back of a ground vehicle, was mounted atop a 14-ft-tall aluminum frame in order to simulate UAS LiDAR data collection from an elevated position atop an extended telehandler boom. First, the aluminum tower must be fixed to the telehandler's pallet forks via ratchet straps (Figure 14).

Figure 14. Telehandler pallet fork and ratchet-strap mounting system.



Once the tower was securely fastened to the telehandler, the telehandler was lifted and then lowered at an angle to allow for laser mounting (Figure 10). In this position, the laser system can be activated and instrumented for use during data collection. Once laser system setup was complete, the tower was straightened and held at a low boom height to allow for safe telehandler travel to the survey area.

Once at the survey site, the telehandler was run through a dynamic alignment in order to calibrate the IMU. The dynamic alignment consisted

of driving multiple figure-eight patterns while the laser system collected IMU and GPS data. Figure-eights were driven until the IMU heading accuracy reached a threshold of 0.05 deg. Once a satisfactory alignment was reached, the laser system entered a mandatory countdown of 5 min where trajectory data were prepared for precise post processing.

Once the laser system was set up and raised to the proper collection height, data acquisition began. The telehandler legs were kept low but off the ground in the case that wind exceeded equipment limits. Proprietary Riegl data collection software, namely RiAQUIRE, was used to initialize and begin the laser scan. Collection in RiAQUIRE was manually set to start and stop data writing to file every 60 sec. This chunking of the data allowed for more efficient post processing.

The position of the telehandler's driving path was determined by the sweep field of view (FOV) of the laser system while in line-scan mode. The laser system was oriented such that the laser swept horizontally in front of the tower with a FOV of approximately 100 deg. At a height of 50 ft and a scan FOV of 100 deg, the laser system can sweep approximately 120 ft horizontally across the test surface. Varying surface widths at the four survey sites (sand-asphalt, dirt, main runway asphalt, and concrete pad) required different telehandler driving paths. The sand-asphalt runway was approximately 150 ft wide, so that two paths were chosen to the left and right of the center line (Figure 15). The remaining survey areas were less than 120 ft wide and therefore allowed for full data collection in single passes. Data was also collected during the telehandler's return trip for the sake of redundancy in the case that data was corrupted during the first pass.

Following each survey, 3-D point data (.rxp files) and trajectory data (.pof files) were transferred to external storage for post processing. During this process the telehandler boom was lowered, and the laser system was deactivated for use in the next survey.

Figure 15. LiDAR survey path on sand-asphalt surface.



5 Data Analysis

Data from the two collection systems, EO and LiDAR, were analyzed in two distinct ways. Where EO data required photogrammetric reconstruction to reveal properties of the 3-D scene, the LiDAR platform performed an effective reconstruction by analyzing laser return times without the need for complex photogrammetric techniques. These various techniques are discussed in the following section.

5.1 3-D reconstruction

Two 3-D reconstruction software packages were used in this effort: Agisoft Photoscan and Pix4D Mapper. While both software packages provided very similar alignment and ground truthing functionality, they each utilized a proprietary dense reconstruction method. The reconstruction workflow was similar for both software packages with some nuance in how the GCPs were applied.

5.1.1 Agisoft Photoscan workflow

5.1.1.1 *Add photos*

Photos from takeoff and landing were not considered for the reconstruction. Once all survey photos were imported, blurry or defective images were either removed or disabled.

5.1.1.2 *Align photos*

Photo alignment accuracy was determined by how much of the original image resolution was used during feature detection. For the purpose of expedient alignment, only half image resolution was used (medium accuracy setting in Agisoft). If GPS metadata are present in the images, reference preselection is available.

5.1.1.3 *Import GCPs*

GCP locations in UTM coordinates were imported as a Comma Separated Value (CSV) file. The GCP location coordinate system was selected before import.

5.1.1.4 Mark GCPs

Once GCP coordinates were imported, they were manually identified and marked in two to three photos per GCP. If the alignment step is completed before marking GCPs, Agisoft will estimate the remaining positions of the GCPs.

5.1.1.5 Optimize photos using GCPs

Photo alignment optimization was available once GCPs were marked in at least two images. Optimizing the alignment of photos with GCP data facilitated the proper scaling and georeferencing of the reconstructed 3-D scene.

5.1.1.6 Build dense cloud

Pixel-level dense reconstruction was performed using the proprietary Agisoft algorithm. Customizability was limited here to choosing only the relative density of the resultant dense point cloud from High to Low. For the purposes of this research, medium- and high-density point clouds were chosen.

5.1.1.7 Generate DEM

Once a dense point cloud was constructed, a high-resolution digital elevation model or surface was interpolated using Agisoft's proprietary method.

5.1.1.8 Generate orthomosaic

The final data product was a georeferenced orthomosaic generated from the DEM using Agisoft's proprietary method.

5.1.2 Pix4D Mapper workflow

5.1.2.1 Add photos

Photos from UAS takeoff and landing as well as any blurry or defective images were removed prior to import. On import, the input and output (same as GCP) coordinate systems were chosen.

5.1.2.2 Import GCPs

GCP locations in UTM coordinates were imported as a CSV file. The GCP location coordinate system was selected before import.

5.1.2.3 Align photos

Photo alignment accuracy was determined by how much of the original image resolution was used during feature detection. For the purpose of expedient alignment only half-image resolution was used. If GPS metadata are present in the images, reference preselection is available.

5.1.2.4 Mark GCPs

Using Pix4D's GCP basic editor, GCPs were marked in two to three photos per GCP. Once this process was completed for all GCPs, the GCP ray editor was used to check Pix4D's estimation of the remaining GCP image positions.

5.1.2.5 Optimize photos using GCPs

Photo alignment optimization was available once GCPs were marked in at least two images. Optimizing the alignment of photos with GCP data facilitated the proper scaling and georeferencing of the reconstructed 3-D scene.

5.1.2.6 Build dense cloud

Pixel-level dense reconstruction was performed using the proprietary Pix4D algorithm. Customizability was limited here to choosing only the relative density of the resultant dense point cloud from High to Low. For the purposes of this work, medium- and high-density point clouds were chosen.

5.1.2.7 Generate DEM

Once a dense point cloud was constructed, a digital elevation model or surface was interpolated using Pix4D's proprietary method.

5.1.2.8 Generate orthomosaic

The final data product was a georeferenced orthomosaic generated from the DEM using Pix4D's proprietary method.

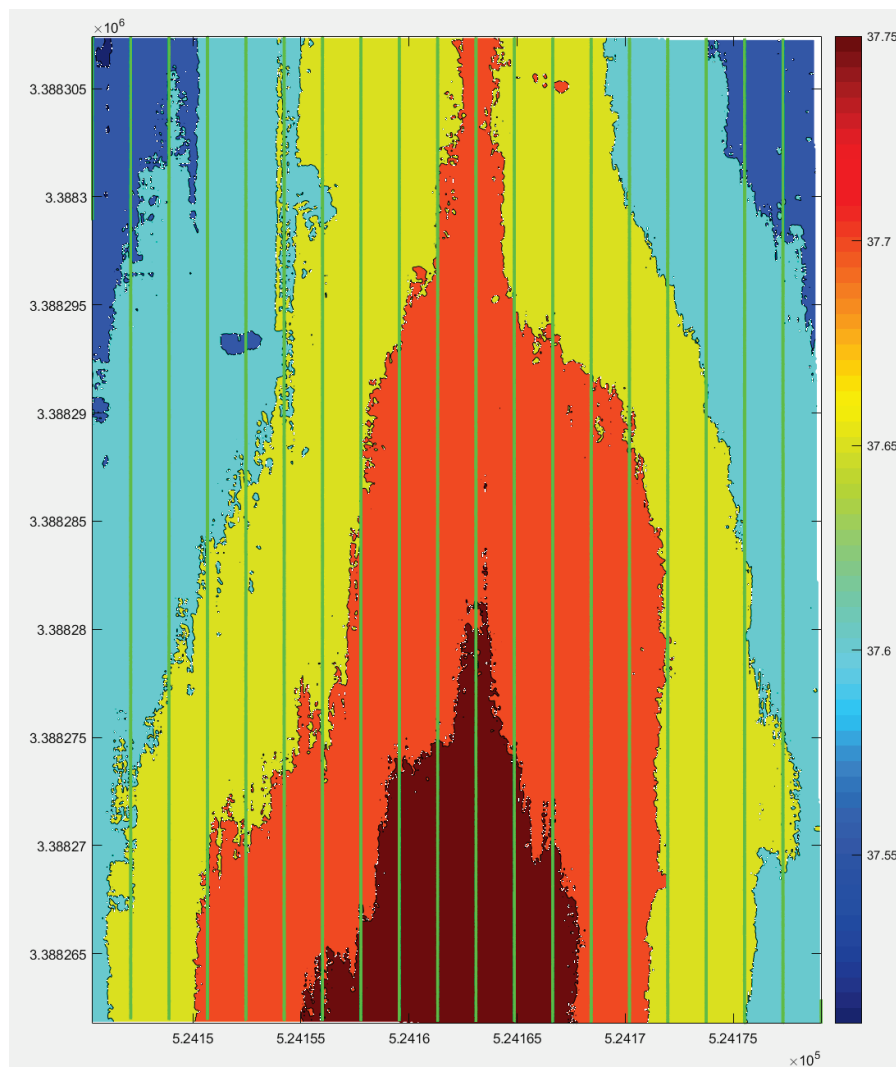
5.2 LiDAR post processing

Post processing was performed on LiDAR data in an effort to georeference the collected point data (.rxp files) using collected trajectory data (.pof files). POSPac MMS software was used for precise post processing of all collected LiDAR data. The POSPac software triangulated and adjusted the position information in the trajectory data based on GPS data collected from a fixed Trimble base station. GPS data were collected in the UTM meters global coordinate system. The UTM meters coordinate system allows for point data to be measured directly in units of meters. The post-processing software also included GPS corrections based on satellite positions. The post-processed trajectory data were then applied to the point data using Riegl's proprietary software, RiPROCESS. The RiPROCESS software combines the raw point data with the corrected trajectory data to produce a highly precise georeferenced LiDAR data file (.las).

6 Results

Cross-sectional data were collected from representative sections of each distinct surface: sand-asphalt, dirt, main runway asphalt, and concrete pad. Due to the small length of the concrete pad (100 ft) and small width of the dirt strip (60 ft), equal length and width sections were not selected for all four surfaces. For comparison between photogrammetric- and LiDAR-based analysis, equivalent cropping was performed for individual surfaces. For each surface, 20 equally spaced cross sections were extracted from the raw point cloud data (Figure 16). In order to reduce the effects of poor reconstruction or partial cross sections, only the middle 18 cross sections were used during analysis.

Figure 16. Cross-section spacing on sample surface.

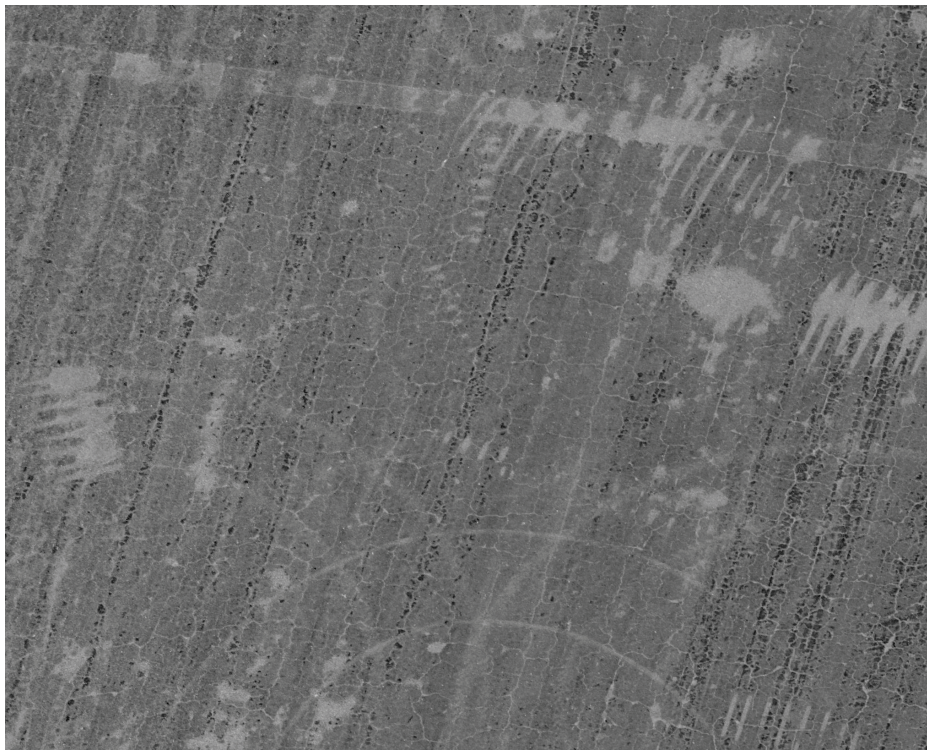


Analysis was performed on the cross-section data using LiDAR point clouds generated by the aforementioned VMZ 2000 and photogrammetric data reconstructed using Photoscan and Pix4D software packages.

6.1 LiDAR analysis

Representative sections from each surface were cropped from raw LiDAR point cloud data (Figure 17). Due to poor EO colorization of the LiDAR data, light intensity colorization was used for LiDAR visualization.

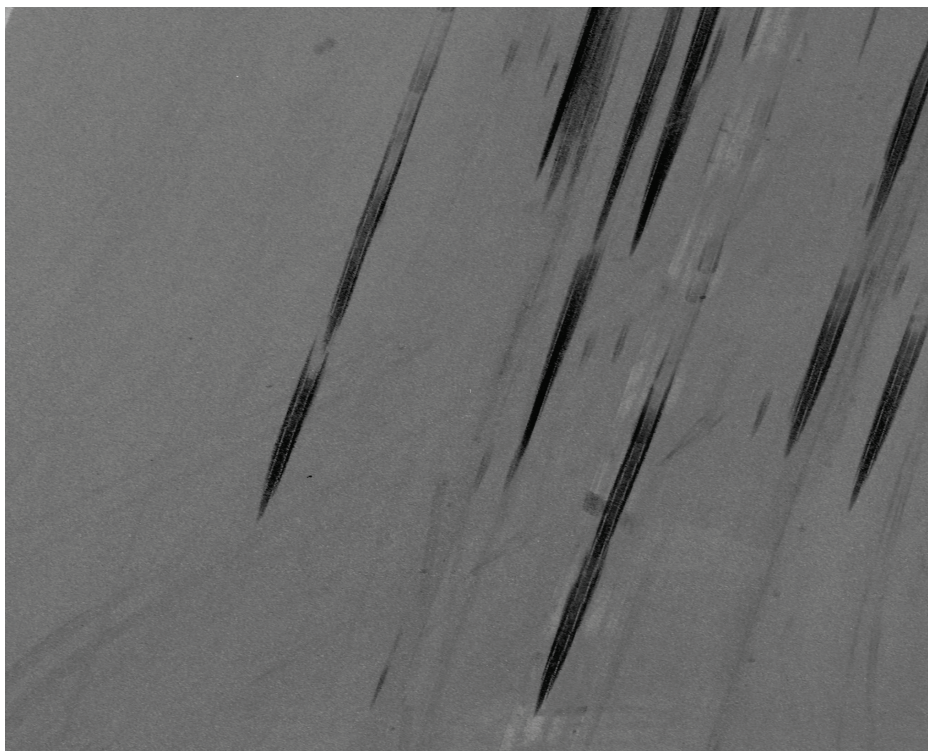
Figure 17. LiDAR data with intensity colorization.



a) Sand-asphalt LiDAR data with intensity colorization.



b) Dirt strip LiDAR data with intensity colorization.



c) Main runway asphalt LiDAR data with intensity colorization.



d) Concrete pad LiDAR data with intensity colorization.

Cross-section data were passed through the FAAs pavement roughness profiling software, ProFAA. Using the ProFAA software, Boeing Bump (dimensionless) and quarter-car IRI (in./mile) roughness indices were generated for each surface. Average cross-section BBI and IRI values for the LiDAR point clouds collected at Camp Rudder are in Table 1.

Table 1. Average BBI and IRI data for Camp Rudder surfaces.

| Parameter | Surface | LIDAR | Photoscan | Pix4D |
|-----------|---------------------|---------|-----------|---------|
| BBI | Sand Asphalt | 0.0301 | 0.0343 | 0.0403 |
| | Dirt Strip | 0.0562 | 0.0636 | 0.0606 |
| | Main Runway Asphalt | 0.0295 | 0.0276 | 0.0296 |
| | Concrete Pad | 0.0235 | 0.0251 | 0.0317 |
| IRI | Sand Asphalt | 24.1000 | 25.7167 | 30.6167 |
| | Dirt Strip | 29.5000 | 44.1167 | 45.1444 |
| | Main Runway Asphalt | 18.1389 | 17.6778 | 20.4167 |
| | Concrete Pad | 16.5333 | 18.9500 | 23.7889 |

From the average BBI and IRI data, it is clear that the LiDAR technique is capable of differentiating between the relatively smooth surfaces, main runway and concrete pad, and the relatively rough surfaces, sand-asphalt and dirt strip. The LiDAR data also show resolution between the highly rough surface, dirt strip, and moderately rough surface, sand-asphalt. Due to the nature of the light-return system, the precise geometric properties of the surface are preserved in the LiDAR point cloud generation. As such, the LiDAR data were considered to be the “ground truth” for all other techniques to be compared against.

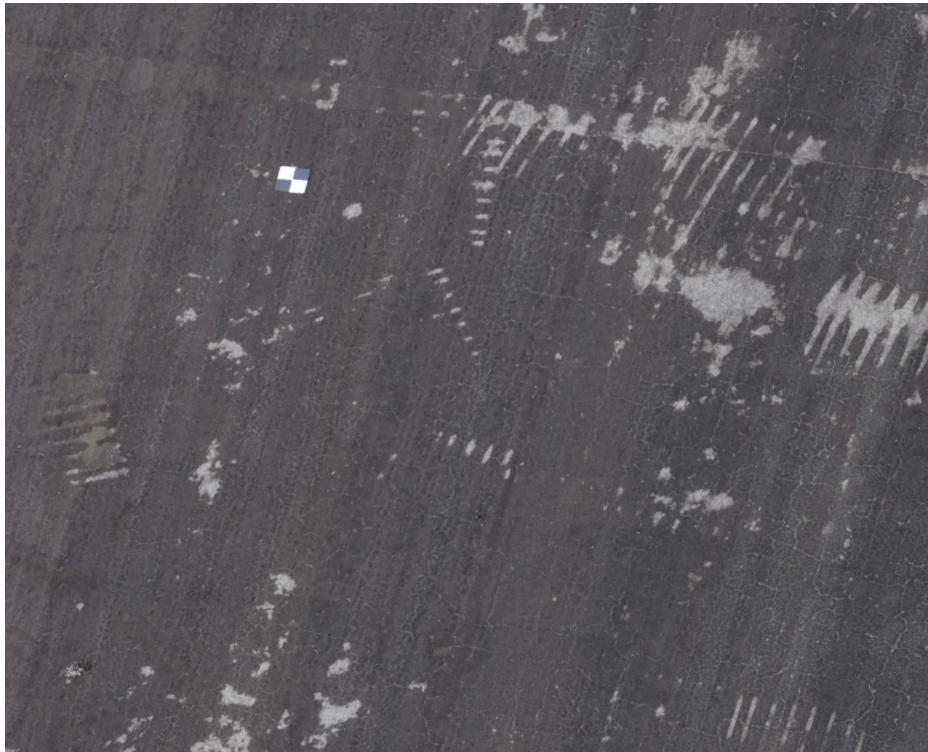
6.2 Photogrammetry analysis

Much like the LiDAR data analysis detailed in Section 6.1, photogrammetry-based reconstructions were compared against the known relative roughness of four distinct surfaces. Individual 3-D reconstruction techniques were also compared directly against LiDAR point clouds to determine deviation from approximate ground truth. For a single surface, high- and medium- resolution reconstructions were compared against each other.

6.2.1 Photoscan reconstruction

The same representative sections selected for the LiDAR analysis were selected here for the Photoscan analysis (Figure 18). The Sony A6000 EO sensor allowed for easy EO colorization of photogrammetric point clouds and was used to visualize the point clouds.

Figure 18. Photoscan data with EO colorization.



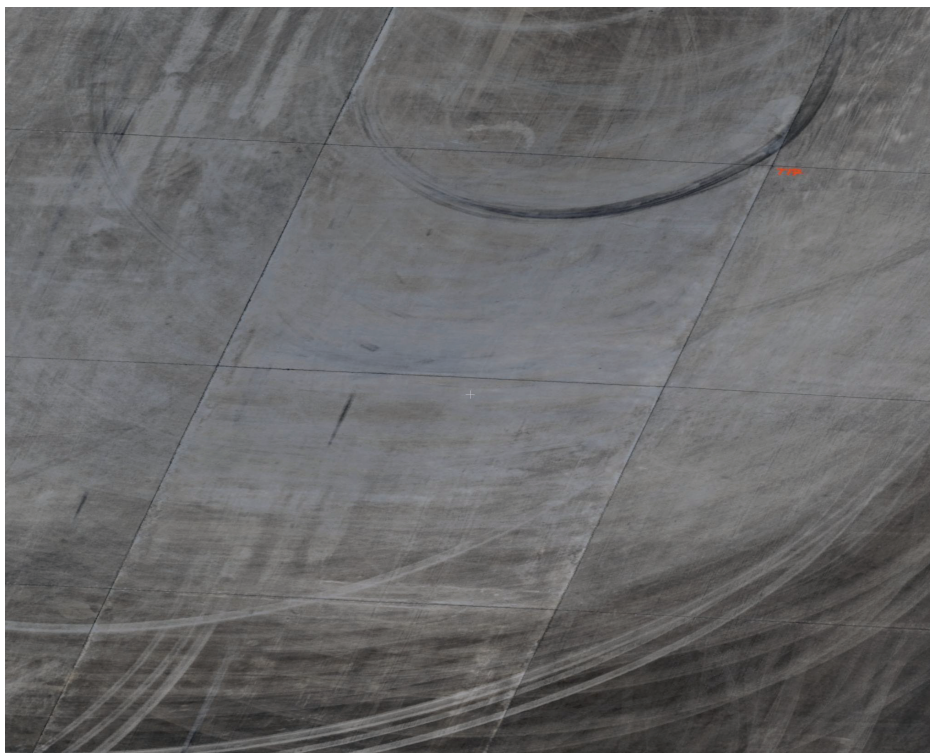
a) Sand-asphalt Photoscan data with EO colorization.



b) Dirt strip Photoscan data with EO colorization.



c) Main runway asphalt Photoscan data with EO colorization.



d) Concrete pad Photoscan data with EO colorization.

Cross-section data, processed in ProFAA, yielded BBI and IRI values for each surface. Averaged BBI and IRI data for the Photoscan technique are in Table 1. Like the LiDAR data, the Photoscan reconstructions were able to both differentiate between smooth and rough surfaces and also showed resolution between moderately and highly rough surfaces. Photoscan reconstruction deviation from LiDAR data was quantified in two ways: linear correlation coefficient of determination (COD) and relative root mean squared error (rRMSE). The COD parameter describes the candidate reconstruction's relative accuracy to ground truth, and the rRMSE parameter determines order of magnitude accuracy of the candidate reconstruction. Data derived from COD and rRMSE analyses for the Photoscan reconstructions are in Table 2.

Table 2. Photogrammetry analysis COD and rRMSE values.

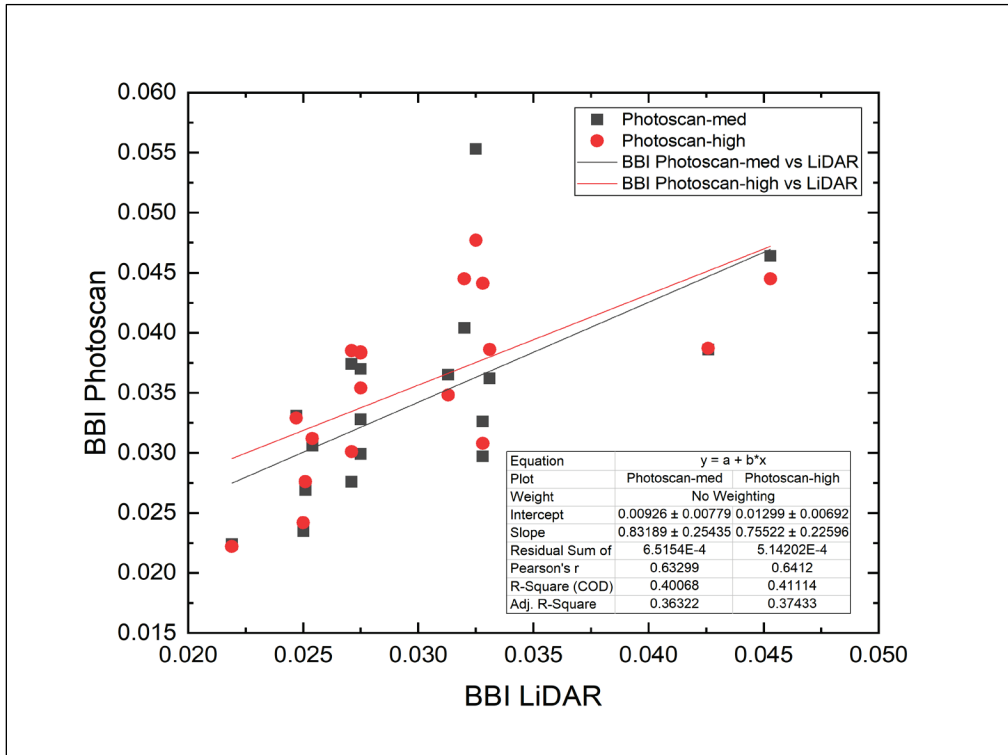
| Surface | Parameter Type | Data Type | COD | rRMSE (%) |
|---------|----------------|----------------|------|-----------|
| SA | BBI | Photoscan-med | 0.40 | 24.6 |
| | | Photoscan-high | 0.41 | 26.3 |
| | | Pix4D-med | 0.28 | 43.5 |
| | | Pix4D-high | 0.31 | 45.1 |
| | IRI | Photoscan-med | 0.77 | 14.6 |
| | | Photoscan-high | 0.70 | 16.2 |
| | | Pix4D-med | .056 | 32.3 |
| | | Pix4D-high | 0.68 | 30.5 |
| DS | BBI | Photoscan | 0.92 | 15.4 |
| | | Pix4D | 0.12 | 13.9 |
| | IRI | Photoscan | 0.84 | 49.7 |
| | | Pix4D | 0.07 | 60.6 |
| MR | BBI | Photoscan | 0.55 | 12.7 |
| | | Pix4D | 0.15 | 16.9 |
| | IRI | Photoscan | 0.79 | 7.6 |
| | | Pix4D | 0.26 | 21.3 |
| CP | BBI | Photoscan | 0.52 | 20.2 |
| | | Pix4D | 0.09 | 48.4 |
| | IRI | Photoscan | 0.30 | 21.1 |
| | | Pix4D | 0.10 | 48.9 |

For the sand-asphalt surface, linear correlation between LiDAR and Photoscan data using the BBI parameter was poor (Figure 19a), yielding CODs of 0.40 and 0.41 for medium- and high-density Photoscan point clouds, respectively. Photoscan correlation to LiDAR data was better using the IRI parameter (Figure 19b), yielding CODs of 0.77 and 0.70 for medium- and high-density Photoscan point clouds, respectively.

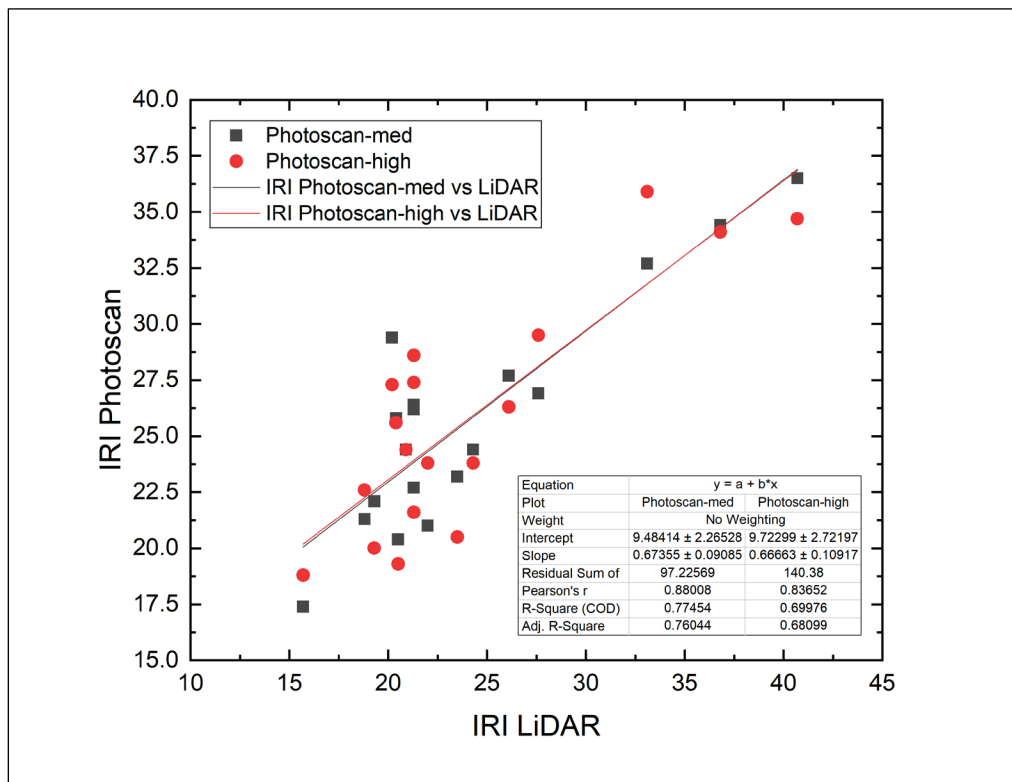
Higher density reconstruction using the Photoscan software did not yield better correlation to LiDAR data. Medium-density reconstructions also reported a similar rRMSE value (24.6%) to that of the high-density reconstruction (26.3%) using BBI. Using the IRI parameter, rRMSE values of 14.6% and 16.2% were measured for the medium- and high-density reconstructions, respectively. Due to the time-consuming nature of high-density photogrammetric reconstructions, medium-density reconstructions were used for the remaining surfaces.

For the dirt-strip surface, high correlation was found between LiDAR and Photoscan data for both the BBI (Figure 20a) and IRI (Figure 20b) parameters yielding CODs of 0.92 and 0.84, respectively. While CODs for the two parameters were similar, rRMSE values showed significant differences contrary to the sand-asphalt results: 15.4% for BBI and 49.7% for IRI. The stark difference in IRI rRMSE values between the sand-asphalt and dirt surfaces is either indicative of an over-representation of roughness in the IRI parameter or an under-representation of roughness in the BBI parameter.

Figure 19. Photoscan vs. LiDAR data using BBI and IRI on sand-asphalt.

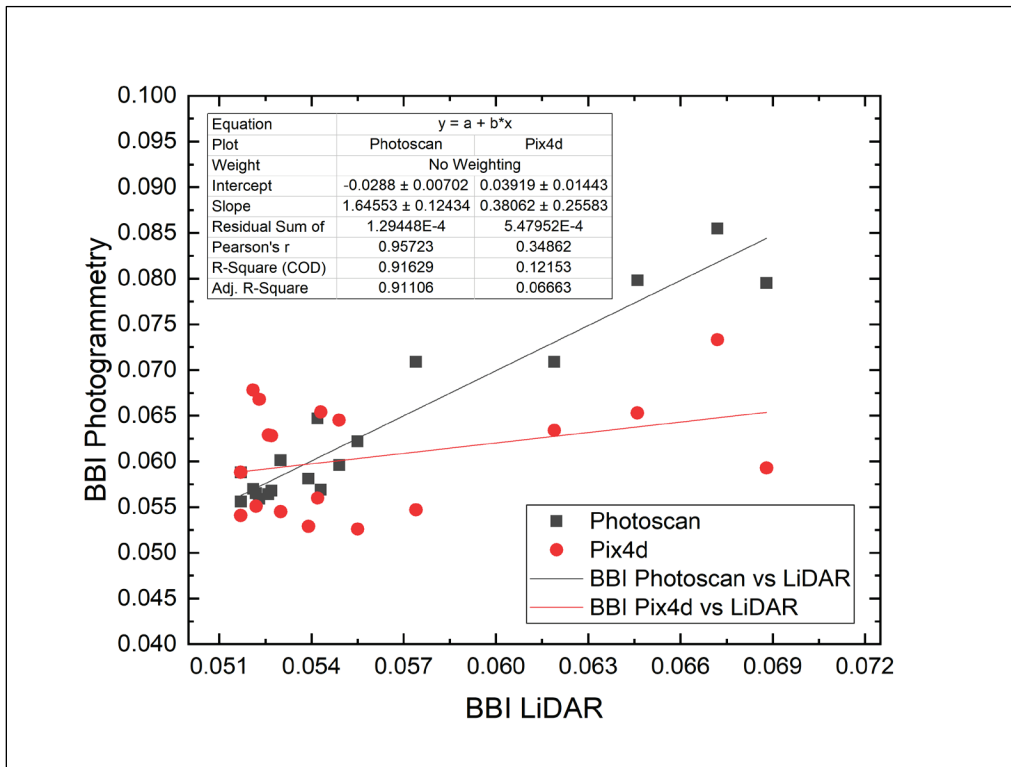


a) Photoscan vs. LiDAR data using BBI at medium and high density on sand-asphalt.

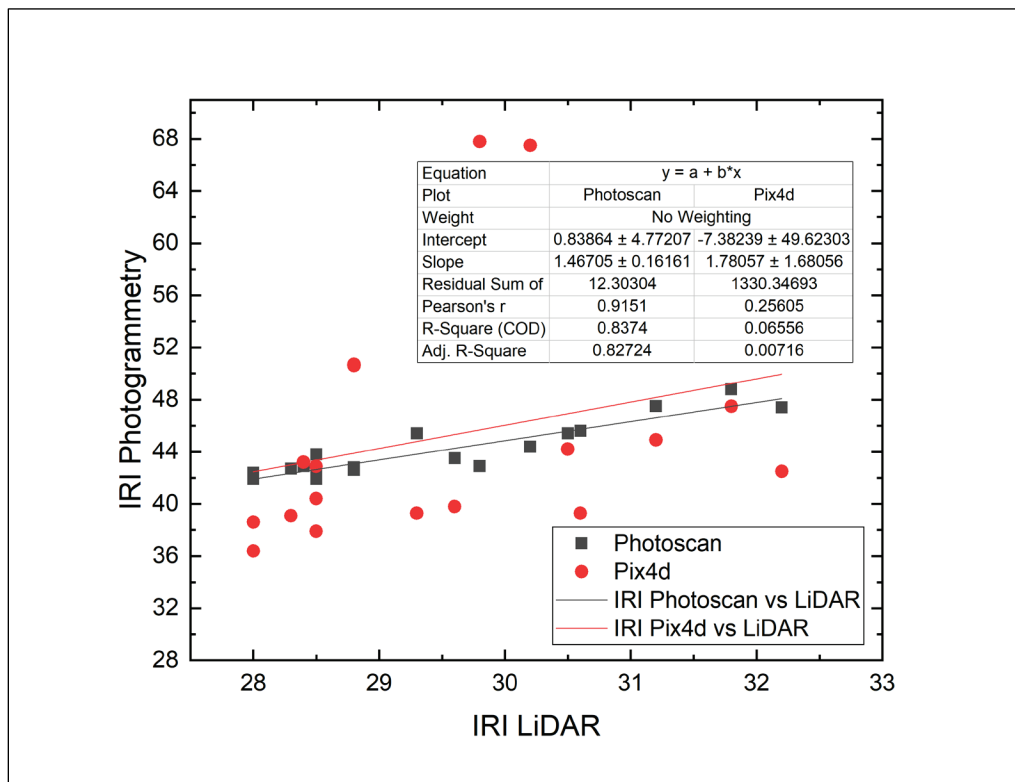


b) Photoscan vs. LiDAR data using IRI at medium and high density on sand-asphalt.

Figure 20. Photogrammetry vs. LiDAR using BBI and IRI on dirt.



a) Photoscan vs. LiDAR and Pix4D vs. LiDAR using BBI on dirt.

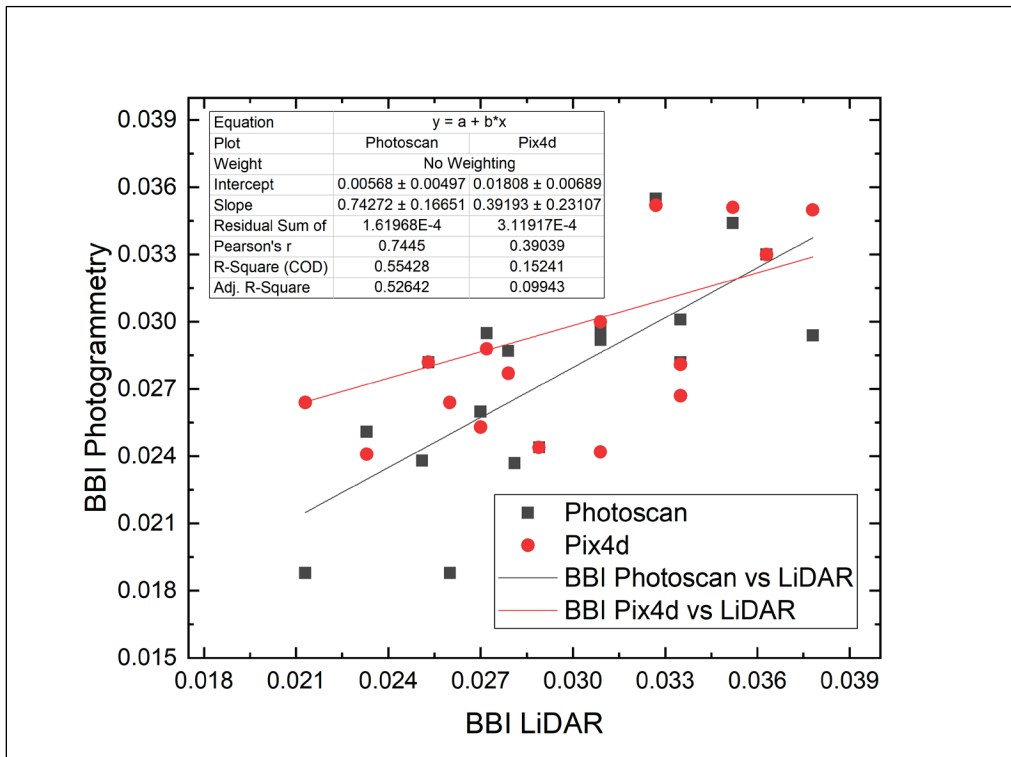


b) Photoscan vs. LiDAR and Pix4D vs. LiDAR using IRI on dirt.

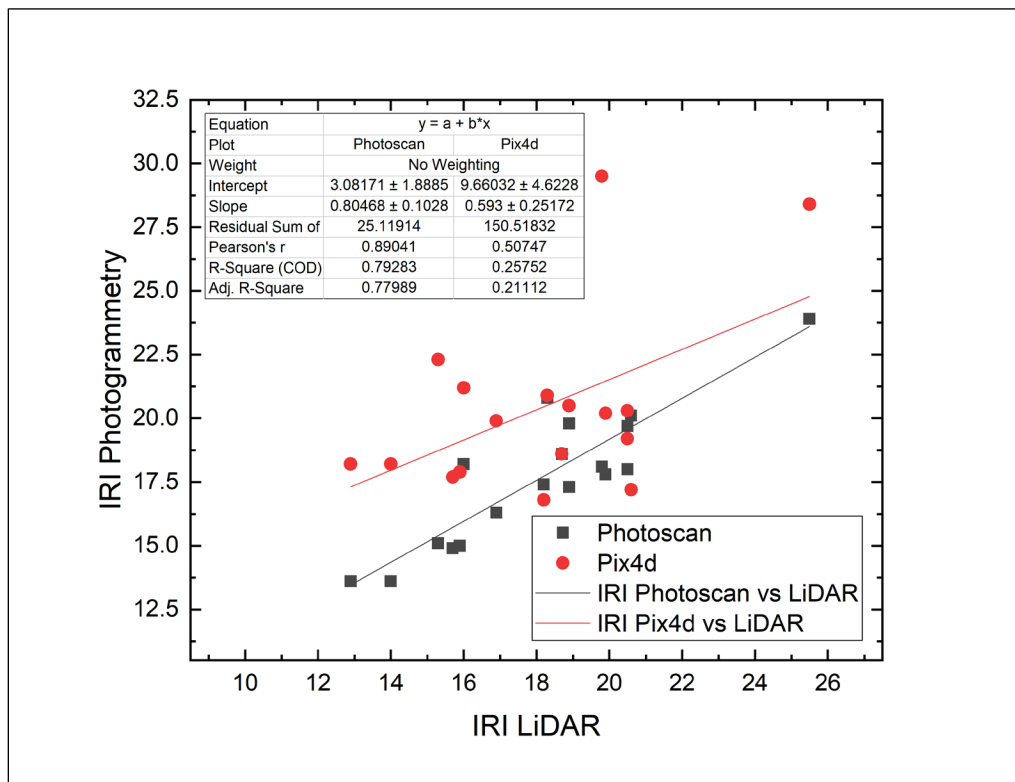
For the main runway asphalt surface, the same analysis was conducted. Correlation between LiDAR and Photoscan data was poor using the BBI parameter (Figure 21a) and acceptable when using the IRI parameter (Figure 21b), yielding CODs of 0.55 and 0.79, respectively. The BBI-based rRMSE value for this surface (12.7%) was approximately half that of the sand-asphalt surface for the medium-density Photoscan reconstruction. The same was true for the IRI-based rRMSE value of 7.6%.

Finally, for the concrete pad surface, poor correlation was found between LiDAR and Photoscan techniques using both BBI (Figure 22a) and IRI (Figure 22b) parameters. Linear CODs for BBI and IRI were 0.52 and 0.30, respectively. Calculated rRMSE values were similar for both BBI and IRI parameters: 20.2% for BBI and 21.1% for IRI.

Figure 21. Photogrammetry vs. LiDAR using BBI and IRI on main runway asphalt.

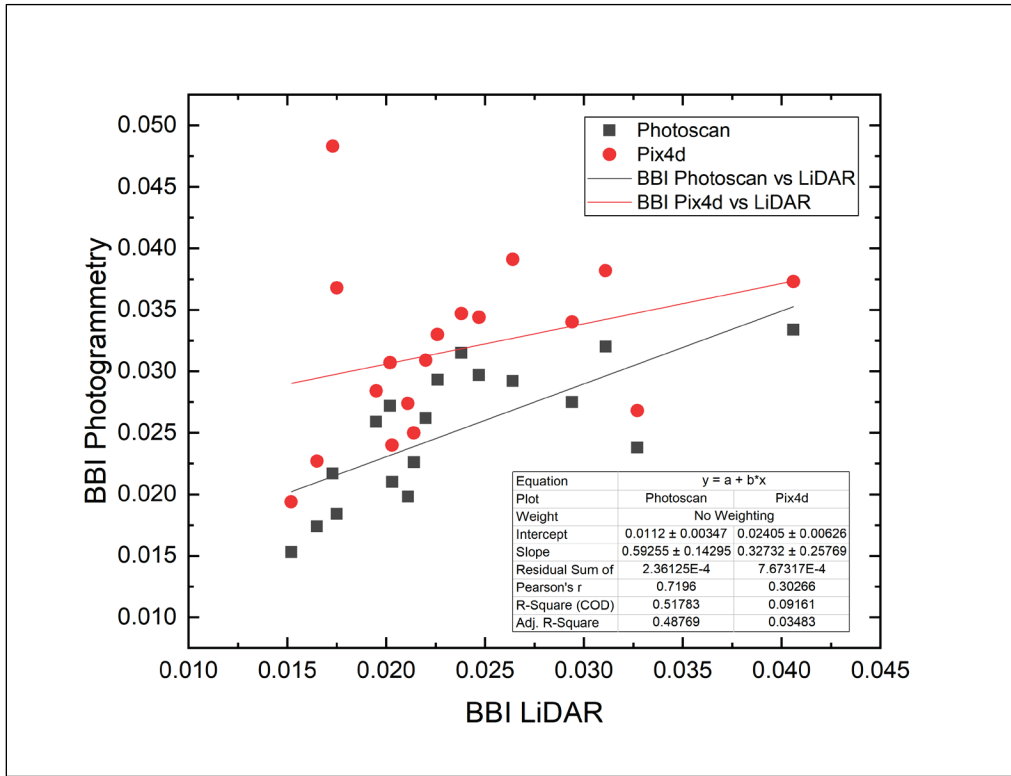


a) Photoscan vs. LiDAR and Pix4D vs. LiDAR using BBI on main runway asphalt.

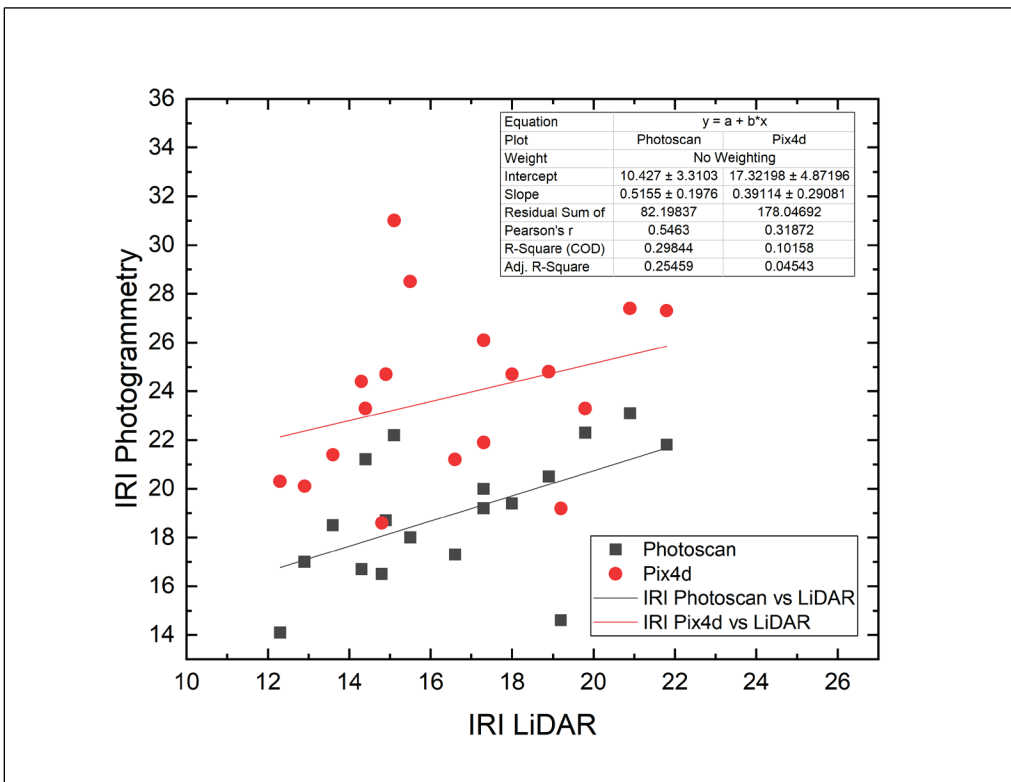


b) Photoscan vs. LiDAR and Pix4D vs. LiDAR using IRI on main runway asphalt.

Figure 22. Photogrammetry vs. LiDAR using BBI and IRI on concrete.



a) Photoscan vs. LiDAR and Pix4D vs. LiDAR using BBI on concrete.

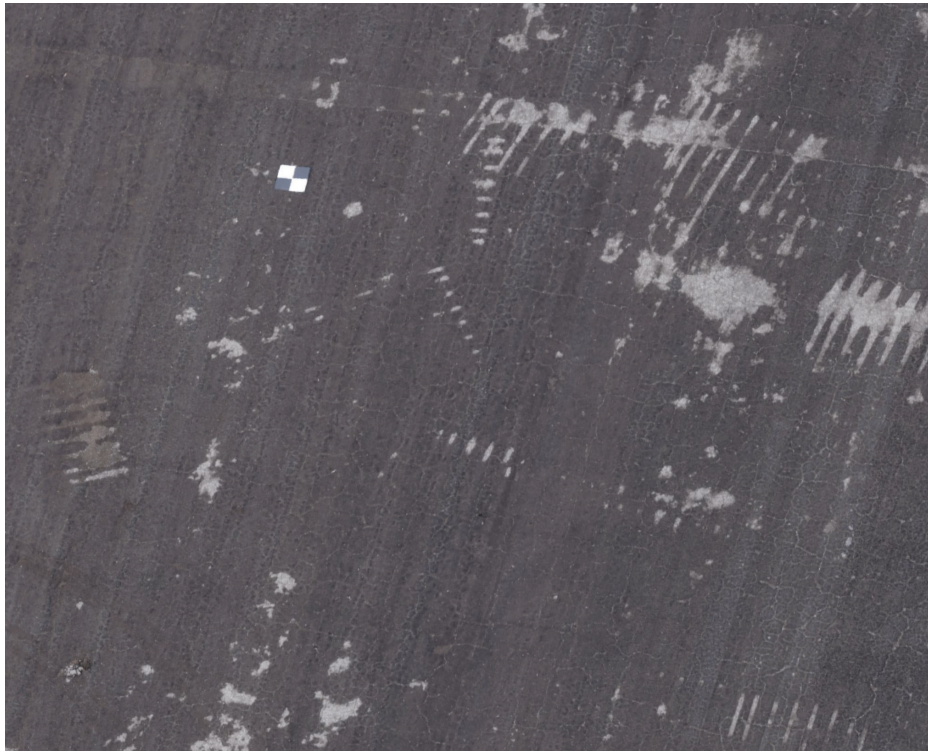


b) Photoscan vs. LiDAR and Pix4D vs. LiDAR using IRI on concrete.

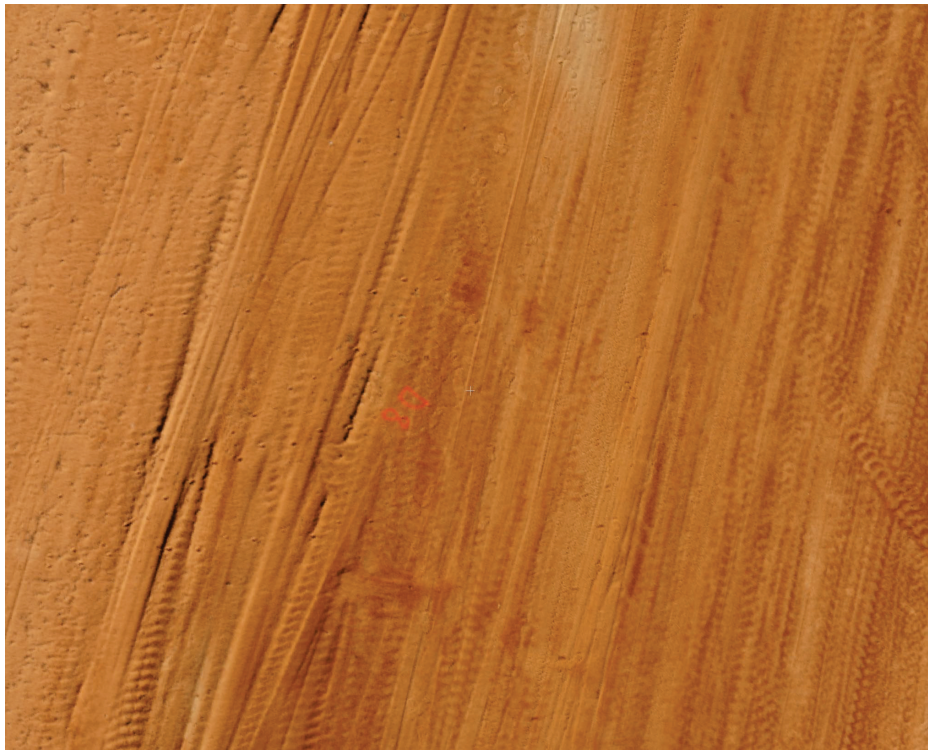
6.2.2 Pix4D reconstruction

Much like the Photoscan analysis, the same representative sections used in the LiDAR analysis were cropped from the Pix4D point clouds (Figure 23). The EO colorization of the Pix4D point clouds was comparable to that of the Photoscan point clouds and thus was used here to visualize the Pix4D data.

Figure 23. Pix4D data with EO colorization.



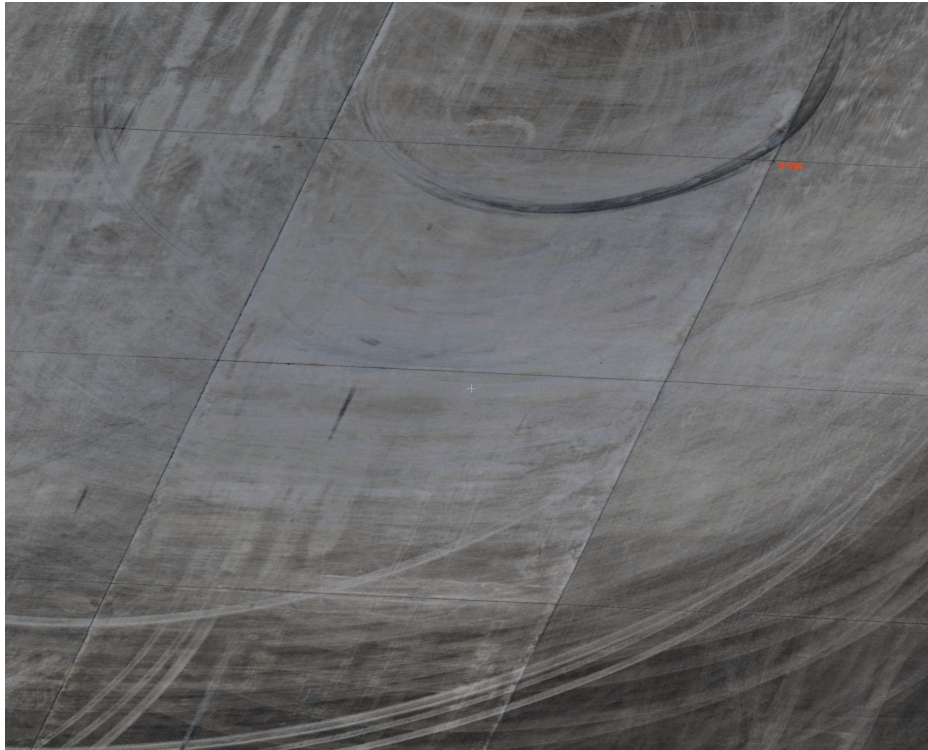
a) Sand-asphalt Pix4D data with EO colorization.



b) Dirt strip Pix4D data with EO colorization.



c) Main runway asphalt Pix4D data with EO colorization.

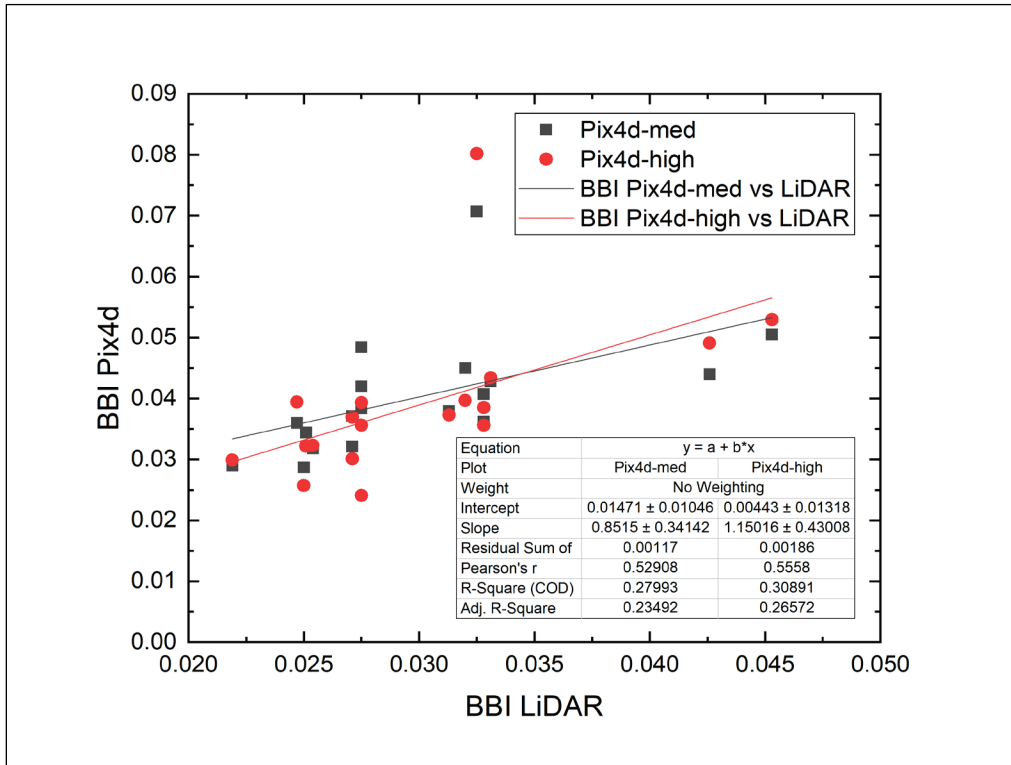


d) Concrete pad Pix4D data with EO colorization.

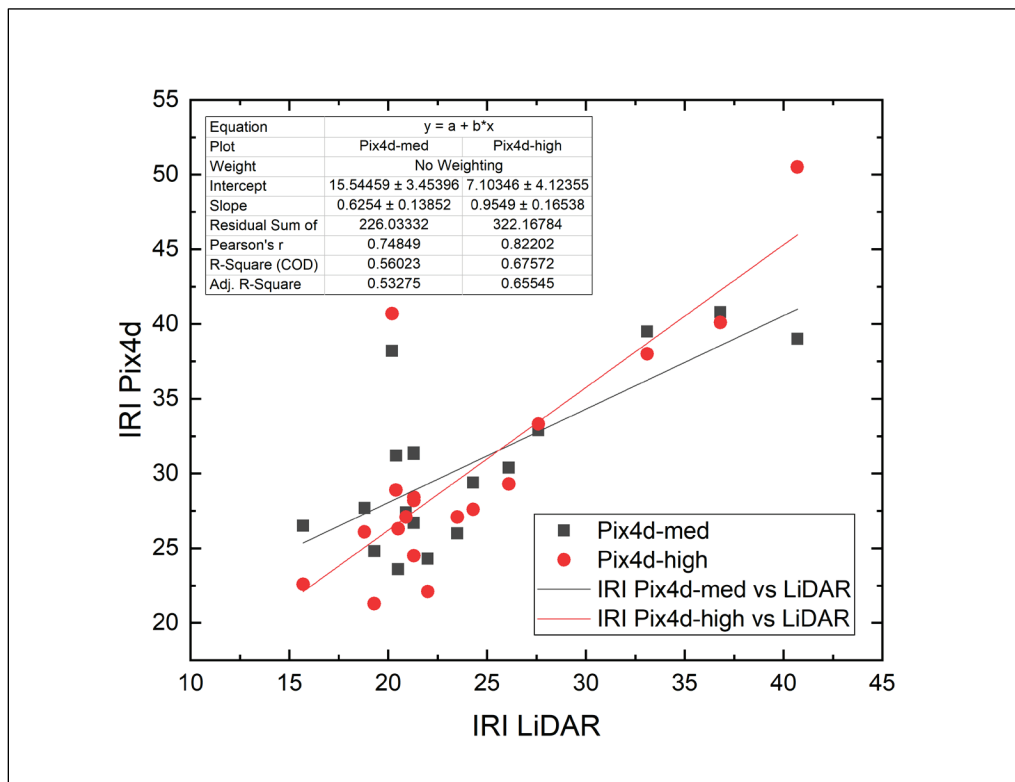
Uniform cross sections were again used to generate BBI and IRI parameters via the ProFAA tool. Averaged BBI and IRI data for the Pix4D technique are in Table 1. Like the previous two techniques, the Pix4D reconstructions were able to differentiate between both smooth and rough surfaces and to also show resolution between moderately and highly rough surfaces. Linear COD and rRMSE parameters were also used to quantify Pix4D correlation to LiDAR data. Data derived from COD and rRMSE analysis for the Pix4D reconstructions are in Table 2.

For the sand-asphalt surface, CODs for both BBI and IRI parameters were poor; however, IRI cross sections again produced better correlations than BBI cross sections. Using the BBI data (Figure 24a), CODs of 0.28 and 0.31 were found for medium- and high-density Pix4D reconstructions, respectively. IRI-based CODs (Figure 24b) of 0.56 and 0.68 were found for medium- and high-density Pix4D reconstructions, respectively.

Figure 24. Pix4D vs. LiDAR data using BBI and IRI on sand-asphalt.



a) Pix4D vs. LiDAR data using BBI at medium and high density on sand-asphalt.



b) Pix4D vs. LiDAR data using IRI at medium and high density on sand-asphalt.

Similar to the Photoscan data, higher density Pix4D reconstructions did not yield better correlation to LiDAR data. High-density reconstructions again reported similar rRMSE values for medium- and high-density reconstructions. Using the BBI parameter, rRMSE values of 43.5% and 45.1% were found for medium- and high-density Pix4D point clouds, respectively. Using the IRI parameter, slightly lower rRMSE values of 32.3% and 30.5% were found for medium- and high-density Pix4D point clouds, respectively. Due to diminishing returns from higher density 3-D reconstruction using the Pix4D method, medium-density point clouds were used for the remaining surfaces.

For the dirt strip surface, poor correlation was found between LiDAR and Pix4D data for both BBI (Figure 20a) and IRI (Figure 20b) parameters with CODs of 0.12 and 0.07, respectively. Similar to the rRMSE response with Photoscan, rRMSE values for Pix4D were found to be 13.9% and 60.6% for BBI and IRI, respectively.

On the main runway asphalt surface, poor correlation was again found for both BBI (Figure 21a) and IRI (Figure 21b) parameters with CODs of 0.15 and 0.26, respectively. As with the Photoscan analysis, Pix4D rRMSE values were found to be approximately half of those for the sand-asphalt surface: 16.9% for BBI and 21.3% for IRI.

Finally, on the concrete pad surface, poor correlation was found using both the BBI (Figure 22a) and IRI (Figure 22b) parameters with CODs of 0.09 and 0.10, respectively. Calculated rRMSE values were approximately the same for both BBI and IRI parameters: 48.4% for BBI and 48.9% for IRI.

7 Conclusions and Recommendations

The photogrammetric-based testing detailed here reveals a number of useful conclusions unique to surface roughness measurements. The present study also echoes some concerns regarding photogrammetric accuracy at small (cm) scales. Two key conclusions were reached during the analysis. First, the Photoscan technique exhibits superior accuracy compared to the Pix4D technique. Second, the Photoscan 3D reconstruction process provides sufficiently accurate surface profiles for use in roughness measurements. It has been determined that while sufficient for roughness measurement, improved photogrammetric accuracy for both the Photoscan and Pix4D techniques is limited by the EO sensor (Sony A6000) and lens (16-50 mm variable) used during testing. Specific conclusions of interest are detailed below.

7.1 Conclusions

- Results detailed in Section 6.1 show that LiDAR data are highly precise (high ground resolution) and capable of differentiating between smooth and rough surfaces with high fidelity consistent with the expected accuracy of laser return time systems.
- Acceptable to good CODs (0.7 to 0.9) in Figure 19b, Figure 20b, and Figure 21b show high linear correlation between Photoscan reconstructions and LiDAR data using the IRI parameter on all but the concrete surface. This indicates two things. First, similar IRI values reveal that Photoscan surface reconstructions on all but the concrete surface are accurate to the real-world surface. Second, poor correlation on the concrete surface shows that, on highly flat and uniform surfaces, the Photoscan technique requires a higher fidelity EO sensor (camera and lens) than the one selected for this effort. It should be noted that poor correlation on the smooth concrete surface may also be due to subpar feature detection common on smooth, featureless surfaces.
- Linear correlations shown in Figure 19 (Photoscan) and Figure 24 (Pix4D) indicate that higher density reconstructions do not provide higher fidelity surface profiles. It is likely that increased reconstruction density is much less important than increased fidelity in the EO sensor itself.
- Poor CODs (less than 0.7) in Figure 20, Figure 21, Figure 22, and Figure 24 indicate that the Pix4D reconstruction method is unacceptable for precise roughness measurement using both BBI and

IRI parameters. While this reveals that the technique is poor in accurately reproducing real-world surfaces at the scale necessary for roughness measurement, low rRMSE values listed throughout Section 6.2.2 indicate that the Pix4D technique is capable of reporting roughness at the correct order of magnitude.

7.2 Recommendations

It is recommended that the Photoscan-based photogrammetric reconstruction technique described here be further tested with higher fidelity EO sensor packages and on more varied surfaces. Should this technique be fielded on active airfields, it is recommended that sub-cm ground control be attained for accurate georeferencing of photogrammetry data products. Any use of this technique should take great care with attaining accurate and clean 2-D imagery. Image blurriness at the level of surface deformities will negatively impact the photogrammetric reconstruction. Finally, it is recommended that further testing be performed to correlate the photogrammetric technique described here to existing profilographs and inertial profilers so that the technique can be directly correlated to ASTM and/or AASHTO accepted methods.

References

- Bay, H., A. Ess, T. Tuytelaars, and L. Van Gool. 2008. *Computer vision and image understanding (CVIU)* 110(3):346-359.
- DeBord, K. J. 1995. *Runway roughness measurement, quantification, and application – the Boeing method*. Document # D6-81746. Seattle, WA: Boeing Commercial Airplane Group Airport Technology Organization.
- FAA. 2009. *Guidelines and procedures for measuring airfield pavement roughness*. Advisory Circular 150/5380-9. Washington, DC: Federal Aviation Administration.
- Fischler, M. A., and R. C. Bolles. 1980. Random sampling consensus: a paradigm model fitting with applications to image analysis and automated cartography. *Communications of the ACM* 24:381-395.
- Furukawa, Y., and C. Hernandez. 2015. Multi-view stereo: a tutorial. *Foundations and Trends in Computer Graphics and Vision* 9(1-2):1-148.
- Goyer, G. G., and R. Watson. 1963. The laser and its application to meteorology. *Bulletin of the American Meteorological Society* 44(9):564-570.
- Leutenegger, S., M. Chli, and R. Siegwart. 2011. BRISK: Binary robust invariant scalable keypoints. In *Proceedings of the IEEE International Conference, ICCV. 6-13 November*. Barcelona, Spain.
- Lowe, David G. 1999. *Object recognition from local scale-invariant features*. In *Proceedings of the International Conference on Computer Vision. 2, 20-27 September, Corfu, Greece*, 1150-1157.
- Maiman, T. H. 1960. Stimulated optical radiation in ruby. *Nature* 187 493-494.
- Rosten, E., and T. Drummond. 2005. *Fusing points and lines for high performance tracking*. In *Proceedings of the IEEE International Conference on computer vision, Vol 2, 17-20 October, Beijing, China*, 1508-1511.
- Sayers, M. W. 1988. *Dynamic terrain inputs to predict structural integrity of ground vehicles*. Wright Patterson Air Force Base, Report No. UMTRI 88-16. Ann Arbor, MI: University of Michigan Transportation Research Institute.
- Sayers, M. W. 1995. *On the calculation of international roughness index from longitudinal road profile*. Transportation Research Record 1501. Washington, DC: Transportation Research Board, National Research Council.
- Triggs, B., P. McLauchlan, R. Hartley, and A. Fitzgibbon. 1999. *Bundle adjustment – a modern synthesis. ICCV '99: Proceedings of the International Workshop on Vision Algorithms, 21-22 September, Corfu, Greece*, 298-372.
- Ullman, S. 1979. The interpretation of structure from motion. *Proceedings of the Royal Society of London* B203:405-426.

- Verhoeven, G., C. Sevara, W. Karel, C. Ressler, M. Doneus, and C. Briese. 2013. New techniques for orthorectification of archaeological aerial frame imagery. In *Good Practice in Archaeological Diagnostics, Natural Science in Archaeology*, ed. C. Corsi, B. Slapsak, F. Vermeulen. Cham, Switzerland: Springer.
- Wallach, H., and D. N. O'Connell. 1953. The kinetic depth effect. *Journal of Experimental Psychology* 45(4):205-217.
- Westoby, M. J., J. Brasington, N. F. Glasser, M. J. Hambrey, and J. M. Reynolds. 2012. 'Structure-from-motion' photogrammetry: a low cost, effective tool for geoscience applications. *Geomorphology* 179:300-314.

REPORT DOCUMENTATION PAGE

Form Approved
OMB No. 0704-0188

Public reporting burden for this collection of information is estimated to average 1 hour per response, including the time for reviewing instructions, searching existing data sources, gathering and maintaining the data needed, and completing and reviewing this collection of information. Send comments regarding this burden estimate or any other aspect of this collection of information, including suggestions for reducing this burden to Department of Defense, Washington Headquarters Services, Directorate for Information Operations and Reports (0704-0188), 1215 Jefferson Davis Highway, Suite 1204, Arlington, VA 22202-4302. Respondents should be aware that notwithstanding any other provision of law, no person shall be subject to any penalty for failing to comply with a collection of information if it does not display a currently valid OMB control number. **PLEASE DO NOT RETURN YOUR FORM TO THE ABOVE ADDRESS.**

| | | | | | |
|--|------------------------------------|--|-----------------------------------|--|--|
| 1. REPORT DATE (DD-MM-YYYY) June 2019 | | 2. REPORT TYPE Final | | 3. DATES COVERED (From - To) | |
| 4. TITLE AND SUBTITLE Assessment of LiDAR- and Photogrammetry-based Airfield Roughness Profiling Techniques | | | | 5a. CONTRACT NUMBER | |
| | | | | 5b. GRANT NUMBER | |
| | | | | 5c. PROGRAM ELEMENT NUMBER | |
| 6. AUTHOR(S) Andrew B. Ward, J. Kent Newman, and G. Bryan Herring IV | | | | 5d. PROJECT NUMBER 465397 | |
| | | | | 5e. TASK NUMBER | |
| | | | | 5f. WORK UNIT NUMBER | |
| 7. PERFORMING ORGANIZATION NAME(S) AND ADDRESS(ES) Geotechnical and Structures Laboratory Coastal and Hydraulics Laboratory U.S. Army Engineer Research and Development Center 3909 Halls Ferry Road Vicksburg, MS 39180-6199 | | | | 8. PERFORMING ORGANIZATION REPORT NUMBER ERDC TR-19-11 | |
| 9. SPONSORING / MONITORING AGENCY NAME(S) AND ADDRESS(ES) U.S. Army Corps of Engineers Washington, DC 20314-1000 | | | | 10. SPONSOR/MONITOR'S ACRONYM(S) USACE | |
| | | | | 11. SPONSOR/MONITOR'S REPORT NUMBER(S) | |
| 12. DISTRIBUTION / AVAILABILITY STATEMENT Approved for public release; distribution is unlimited. | | | | | |
| 13. SUPPLEMENTARY NOTES | | | | | |
| 14. ABSTRACT The measurement of surface roughness is one of the factors necessary for determining stable landing and take-off conditions on airfields. The U.S. Army identified a need for rapid and precise assessment of airfield surface roughness without grossly inhibiting aircraft traffic. The present standard of roughness measurement includes the use of cumbersome ground vehicle-based inertial profilers or slow-speed profilographs. The use of Unmanned Aerial System (UAS) based photogrammetry for remote assessment has been highly successful and the data products derived from these systems are useful to surface roughness measurements. Roughness parameters like the Boeing Bump Index and International Roughness Index can be calculated using 3-D reconstructed surface data derived from photogrammetric techniques. Roughness parameters can also be calculated using the surface obtained by Light Detection and Ranging (LiDAR) systems. While LiDAR techniques are highly accurate and robust, they are often cost-prohibitive. The assessment of photogrammetry-based alternatives to LiDAR systems is required to satisfy airfield roughness measurement needs. Findings herein show that photogrammetric techniques can provide sufficient surface profiles for use in roughness measurement. This report compares multiple photogrammetric software packages for best correlation to actual surface profiles and concludes with a preferred method of surface roughness measurement using UAS-based photogrammetry. | | | | | |
| 15. SUBJECT TERMS Roughness Surface roughness Friction – testing | | Airfield roughness LiDAR Photogrammetry Surface roughness – testing | | Unmanned Aerial System (UAS) Runways (Aeronautics) Safety Optical radar | |
| 16. SECURITY CLASSIFICATION OF: | | | 17. LIMITATION OF ABSTRACT | 18. NUMBER OF PAGES | 19a. NAME OF RESPONSIBLE PERSON |
| a. REPORT Unclassified | b. ABSTRACT Unclassified | c. THIS PAGE Unclassified | | | 19b. TELEPHONE NUMBER (include area code) |